Cell Reports

Dynamic Ca^{2+} sensitivity stimulates the evolved SARS-CoV-2 spike strain-mediated membrane fusion for enhanced entry

Graphical abstract

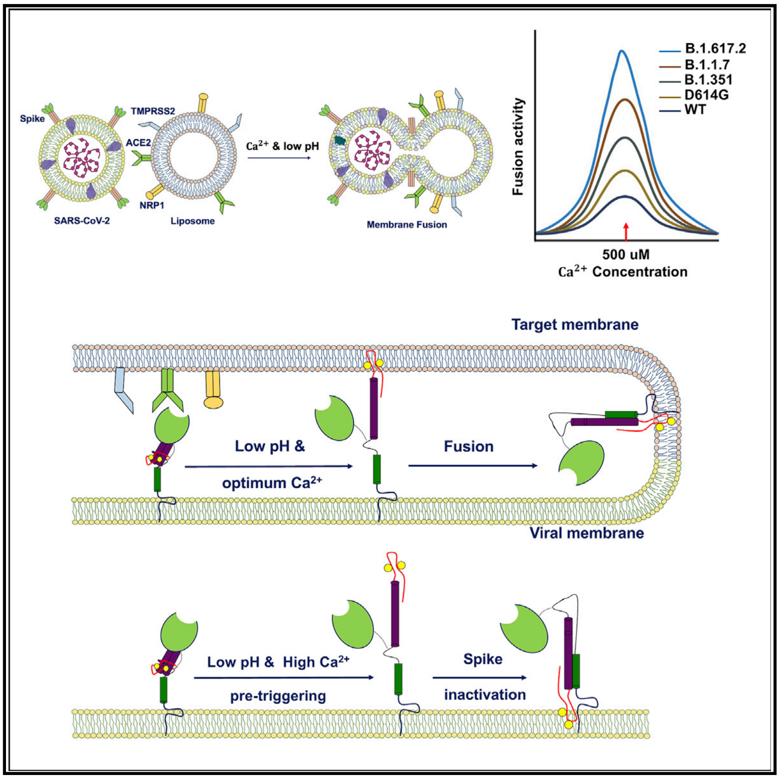

Highlights

- SARS-CoV-2 spike protein is a dynamic calcium sensor
- Ca^{2+} and low pH triggers spike conformational change for membrane fusion
- Evolved spike variants show correlation in calcium sensitivity and fusion activity
- Pre-triggering spike virion with low pH and Ca^{2+} attenuates membrane fusion

Authors

Puspangana Singh, Shreya Mukherji, Swarnendu Basak, Markus Hoffmann, Dibyendu Kumar Das

Correspondence

dkdas@iitk.ac.in

In brief

Singh et al. show that low pH and Ca^{2+} facilitate SARS-CoV-2 spike-driven membrane fusion. Ca^{2+} drives a pre- to post-fusion conformational change of the spike protein. SARS-CoV-2 spike variants of concern have evolved with enhanced dynamic calcium sensitivity, which increases fusion activity and cell entry.

Singh et al., 2022, Cell Reports *39*, 110694
April 19, 2022 © 2022 The Authors.
https://doi.org/10.1016/j.celrep.2022.110694

Cell Reports

CellPress
OPEN ACCESS

Article

Dynamic Ca^{2+} sensitivity stimulates the evolved SARS-CoV-2 spike strain-mediated membrane fusion for enhanced entry

Puspangana Singh,[1] Shreya Mukherji,[1] Swarnendu Basak,[1] Markus Hoffmann,[2,3] and Dibyendu Kumar Das[1,4,5,*]
[1]Department of Biological Sciences and Bioengineering, Indian Institute of Technology Kanpur, Kanpur, Uttar Pradesh 208016, India
[2]Infection Biology Unit, German Primate Center, Kellnerweg 4, 37077 Göttingen, Germany
[3]Faculty of Biology and Psychology, Georg-August-University Göttingen, Wilhelmsplatz 1, 37073 Göttingen, Germany
[4]The Mehta Family Center for Engineering in Medicine, Indian Institute of Technology Kanpur, Kanpur, Uttar Pradesh 208016, India
[5]Lead contact
*Correspondence: dkdas@iitk.ac.in
https://doi.org/10.1016/j.celrep.2022.110694

SUMMARY

Mutations in the spike protein generated a highly infectious and transmissible D614G variant, which is present in newly evolved fast-spreading variants. The D614G, Alpha, Beta, and Delta spike variants of SARS-CoV-2 appear to expedite membrane fusion process for entry, but the mechanism of spike-mediated fusion is unknown. Here, we reconstituted an *in vitro* pseudovirus-liposome fusion reaction and report that SARS-CoV-2 wild-type spike is a dynamic Ca^{2+} sensor, and D614G mutation enhances dynamic calcium sensitivity of spike protein for facilitating membrane fusion. This dynamic calcium sensitivity for fusion is found to be higher in Alpha and Beta variants and highest in Delta spike variant. We find that efficient fusion is dependent on Ca^{2+} concentration at low pH, and the fusion activity of spike dropped as the Ca^{2+} level rose beyond physiological levels. Thus, evolved spike variants may control the high fusion probability for entry by increasing Ca^{2+} sensing ability.

INTRODUCTION

Severe acute respiratory syndrome coronavirus 2 (SARS-CoV-2) has caused the ongoing COVID-19 pandemic (Zhou et al., 2020a). Despite the presence of a proofreading capability in viral replication machinery, the RNA genome of the virus is rapidly evolving and continually accumulating genomic mutations as it transmits (Robson et al., 2020; Li et al., 2020). A variant with a single-residue substitution of aspartic acid with glycine at position 614 of the virus's spike protein (D614G) suddenly became the dominant strain all over the world in 2020 (Korber et al., 2020; Volz et al., 2021; Yurkovetskiy et al., 2020). The putative importance of the D614G spike variant has been observed owing to its high infectivity and enhanced transmissibility in animal models (Plante et al., 2021; Hou et al., 2020).

Following D614G, several variants of concern have emerged, including B.1.1.7 lineage first reported in the United Kingdom (Alpha), the B.1.351 lineage in South Africa (Beta), and the B.1.617.2 lineage in India, also known as Delta variant (Tegally et al., 2020; Grabowski et al., 2021; Mlcochova et al., 2021). All these variants contain the D614G mutation. These new variants are not only fast spreaders but also are more resistant to immunity elicited by the vaccination of Wuhan strain (Wang et al., 2021; Wibmer et al., 2021). The Delta strain has outcompeted all other variants of concern and became the dominant strain worldwide within a few months after its emergence (Mlcochova et al., 2021). The Delta strain has been estimated to be twice as transmissible than previous variants of concern (Earnest et al., 2021; Dagpunar, 2020). Therefore, it is important to understand the mechanism of viral entry for increased transmissibility to design intervention strategies.

The trimeric spike (S) glycoprotein of SARS-CoV-2's surface facilitates membrane fusion for host cell entry and therefore is an important target for development of therapeutics and vaccines. The S protein is processed by a furin-like protease into the receptor-binding subunit S1 and the fusion subunit S2 (Wrapp et al., 2020; Walls et al., 2020). After engagement of the receptor-binding domain (RBD) in S1 on the host cell surface via receptors angiotensin converting enzyme 2 (ACE2) and neuropilin-1 (NRP1) followed by a second proteolytic cleavage within S2 (S2′ site), the S protein undergoes large conformational changes, resulting in dissociation of S1 and large-scale structural refolding of S2 into a post-fusion structure to trigger fusion of the virus and host cell membranes to initiate infection (Hoffmann et al., 2020; Daly et al., 2020; Cantuti-Castelvetri et al., 2020; Cai et al., 2020). But, how the D614G mutation and newly evolved spike variants facilitate the spike conformational change for membrane fusion for enhanced viral infectivity is unknown. Therefore, understanding the role of D614G mutation and newly evolved spike variants in spike protein-mediated membrane fusion for facilitating viral entry is important for developing novel intervention strategies against COVID-19.

Here we focus on membrane fusion enhancement, mediated by SARS-CoV-2 D614G and newly evolved spike variants and compare their fusion efficacy. Recent work has reported that the D614G variant shows increased infectivity by altering the receptor-binding conformation with receptor ACE2 (Yurkovetskiy et al., 2020; Zhang et al., 2020a, 2020b). The D614G spike trimer is reported to sample the RBD up-conformation more frequently than the wild-type (WT) spike, but it binds more weakly to the recombinant ACE2 than the WT. The structural study of D614G trimers revealed the breaking of a salt bridge between D614 and a lysine residue (K854) in the fusion peptide proximal region (FPPR), which may help in clamping the RBD in the pre-fusion up-conformation and also prevent premature dissociation of the G614 trimer, but it does not explain the enhance fusion activity of spike fusion domain of D614G spike variants (Yurkovetskiy et al., 2020; Zhou et al., 2020b; Xiong et al., 2020; Zhang et al., 2021). To resolve these issues, we report here the membrane fusion consequences due to D614G substitution and compare with B.1.1.7, B.1.351, and B.1.617.2 spike variants in the context of the full-length spike protein by reconstituting the fusion between pseudotyped SARS-CoV-2-S virions and proteoliposomes.

A recent report has demonstrated that calcium ion channel blockers can restrict Ebola virus entry and also inhibit SARS-CoV-2 infectivity (Sakurai et al., 2015; Straus et al., 2020a, 2020b). Rubella virus fusion protein was first identified as a calcium-sensitive viral fusion protein (Dubé et al., 2014). Also, calcium plays an important role for Ebola virus glycoprotein (GP)-mediated entry (Das et al., 2020; Nathan et al., 2020). Niclosamide, a potent drug molecule, has been reported to inhibit SARS-CoV-2 spike-mediated syncytia formation by suppressing the activity of a calcium-activated ion channel TMEM16 (Braga et al., 2021). But, how calcium channel blockers impact SARS-CoV-2 infectivity and what is the underlying role of Ca^{2+} ion in spike-mediated membrane fusion for entry is unknown. Most importantly, the role of Ca^{2+} in D614G spike, B.1.1.7, B.1.351, and B.1.617.2 variants mediating membrane fusion for enhanced viral entry is also unknown.

Here, we design a fluorescent labeling platform for *in vitro* reconstitution of the SARS-CoV-2 spike protein-mediated membrane fusion between viral and liposomal membrane to probe the fusion dynamics of the WT spike and D614G spike variants and compare with B.1.1.7, B.1.351, and B.1.617.2 spike variants. ACE2 and NRP1 are the two-receptor proteins known to directly interact with the spike trimeric protein, and serine protease TMPRSS2 primes the spike protein for fusion (Hoffmann et al., 2020; Daly et al., 2020; Cantuti-Castelvetri et al., 2020). We find that these proteins are essential but not enough for membrane fusion. We have identified cellular Ca^{2+} as the catalyzing chemical factor for SARS-CoV-2 spike activation for membrane fusion, and visualizing the mechanism of action is significant because these three interacting molecules, ACE2, NRP1, and TMPRSS2, individually and independently can enhance D614G spike-mediated membrane fusion by interacting directly with spike trimer in the presence of calcium at low pH condition, suggesting the lysosome as the point of entry for the virus. The B.1.1.7 and B.1.351 spike variants show higher membrane fusion efficacy compared to D614G, while B.1.617.2 variant shows the highest calcium-dependent membrane fusion efficiency among all the spike strains. Importantly, the concentration of Ca^{2+} is a key factor for membrane fusion, and fusion is non-monotonically dependent on Ca^{2+} concentration.

Using genetic code expansion techniques, we site specifically incorporated fluorescent-tagged non-canonical amino acids (ncAAs) into the FPPR of S2 domain of spike virions to probe the effect of Ca^{2+} in fusion peptide binding into membrane. We found that D614G spike variant is 150% more sensitive to the physiological Ca^{2+} concentration for fusion peptide binding to target membrane and 100% more fusion efficient compared to WT. Further, we incorporated two ncAAs into the S2 domain of spike protein to probe the role of Ca^{2+} in conformational change of S2 domain using fluorescence resonance energy transfer (FRET) spectroscopy. We found that the high Ca^{2+} sensitivity of D614G spike variants facilitates pre- to post-fusion conformational change of S2 domain, leading to the enhanced membrane fusion efficiency compared to WT spike.

Overall, our findings (1) unravel the fundamental mechanism of SARS-CoV-2 spike-mediated membrane fusion and fusion enhancement mediated by D614G and evolved spike variant of concern, (2) suggest a model in which the Ca^{2+} concentration and low pH is critical for ensuring the efficient spike conformational change for membrane fusion, and (3) suggest that spatiotemporal dynamics of Ca^{2+} are important for viral entry.

RESULTS

Ca^{2+} drives the spike-mediated membrane fusion at low pH

To determine the minimal components required to promote SARS-CoV-2 spike-mediated membrane fusion, we first reconstituted a fluorescence-based *in vitro* virus-liposome membrane fusion assay (Figure 1A). We formed HIV-based SARS-CoV-2 pseudovirions using HIV Gagpol as core and WT human-codon optimized spike protein (Wuhan-hu-1) on the envelop. We performed site-directed mutagenesis on the WT spike to introduce the D614G spike variant. The D614G spike protein expression level in cell and virion was similar to WT spike (Figure S1A). SARS-CoV-2 WT spike or D614G spike variant pseudotyped viral membrane was labeled with a self-quenching concentration of the lipophilic dye DiO. The labeled virions were introduced to proteoliposomes, coated with the recombinant ACE2 (1-615aa) (Figure 1A). No dequenching of DiO was observed at neutral pH 7 for either the WT or D614G variant (Figure 1B) (Figure S1). Decreasing the pH to 6, 5, and 4.6 still resulted in no dequenching of dye, indicating that the presence of ACE2 and low pH are not enough for spike mediating membrane fusion (Figure 1B). Inclusion of a physiological concentration of Ca^{2+} (0.5 mM) into the assay resulted in the DiO dequenching, indicating that membrane fusion happens only in presence of calcium at low pH 4.6 (Figure 1B). D614G spike variant resulted in modest changes in the extent of fusion efficacy increment in presence of ACE2. The resultant fusion efficiency after following the fusion kinetics for 20 min has been shown as the fusion index (Figures 1C and 1D).

Similarly, to determine the individual ability of NRP1 in spike-mediated membrane fusion, we generated liposomes coated with recombinant NRP1-b1 (273-427aa) and reconstituted the

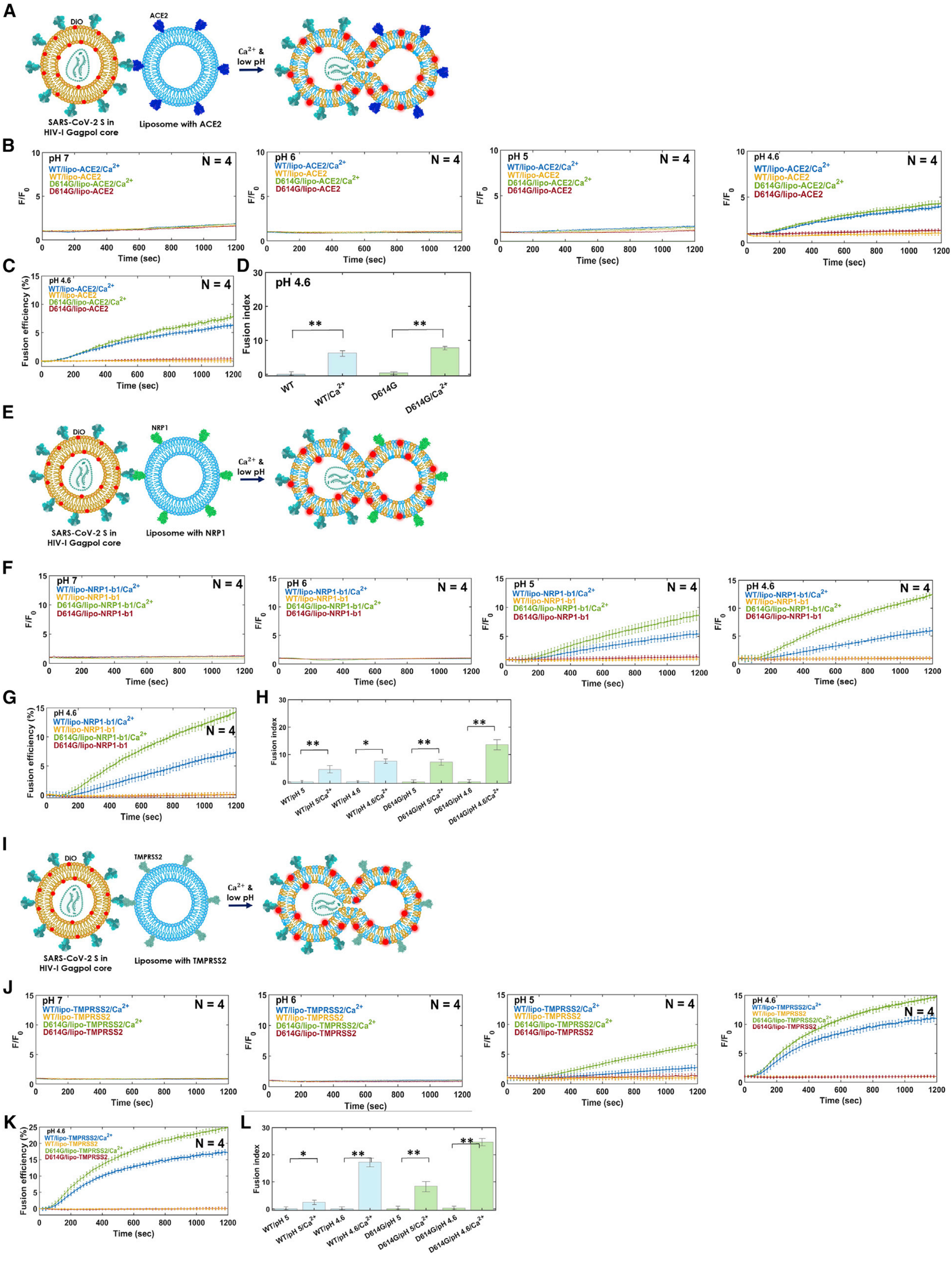

(legend on next page)

pseudovirus-proteoliposome fusion assay (Figure 1E). We found that NRP1-b1 alone cannot facilitate fusion at any given pH range from 7 to 4.6 (Figure 1F). Only after addition of Ca^{2+} (0.5 mM) was spike-mediated membrane fusion observed at pH 5 and 4.6 (Figures 1F and S1). The fusion efficacy at pH 4.6 is higher than at pH 5 in presence of Ca^{2+}, and D614G shows higher fusion efficiency compared to WT spike (Figures 1G and 1H). The fusion efficiency with NRP1 is pronounced compared to ACE2 (2-fold) as indicated in the fusion index (Figure 1H), suggesting that SARS-CoV-2 spike can drive fusion with NRP1 independently, at lysosomal pH in presence of intracellular calcium.

Next, we pursued the individual role of TMPRSS2 in spike-mediated membrane fusion and reconstituted the *in vitro* fusion assay between pseudovirus and recombinant TMPRSS2 (1–492aa) functionalized liposomes (Figure 1I). Similar to the effect observed with recombinant ACE2 and NRP1-b1, we did not observe any fusion events at given pH range from 7 to 4.6 (Figures 1J and S1). Only after inclusion of 0.5 mM Ca^{2+}, fusion was observed at pH 5 and 4.6 (Figure 1K). With TMPRSS2, D614G showed greater fusion efficiency compared to WT spike (Figures 1K and 1L). The individual fusion efficiency with TMPRSS2 was found to be greater compared to ACE2 (4-fold) and NRP1 (2-fold) (Figures 1D, 1H, and 1L). The viral fusogenicity has also been performed in 293T cell lines, expressing full-length ACE2, NRP1, and TMPRSS2, using enzymatic-based β-lactamase assay (STAR Methods) (Cavrois et al., 2002). D614G spike variant is found to be more fusogenic in all conditions and fusion is completely dependent on calcium (Figure S1B). Chelating intracellular calcium of infected cells with BAPTA-AM completely abrogated the viral fusion activity for WT and D614G variants, suggesting Ca^{2+} is an indispensable factor for fusion (Figures S1 and S2).

D614G spike variant shows higher membrane fusion efficiency

To understand the combined effect of the receptors ACE2 and NRP1 and protease TMPRSS2 on spike-mediated membrane fusion, we functionalized the surface of liposomes with all the recombinant ACE2, NRP1-b1, and TMPRSS2 and monitored the virus and liposome fusion at different pH (Figure 2A). No fusion events were observed in the absence of calcium, and control experiments show that spike and receptor interaction drive the membrane fusion at low pH and in the presence of Ca^{2+}(Figure 2B) (Figure S2). Only after inclusion of Ca^{2+} (0.5 mM) is the fusion process triggered at low pH 5 and 4.6. The fusion efficiency at pH 4.6 seems higher than that at pH 5, indicating that low pH assists in conformational refolding of spike for fusion. The combined effect of all the receptors and protease in membrane fusion was modest for the WT spike but found to be enhanced for the D614G variant spike. D614G spike fusion efficiency was found to be double compared to the WT spike (Figures 2C–2E). While comparing the individual role of receptors on fusion, our data suggest that D614G mutation may facilitate receptor engagement or make the spike more prone to triggering for enhanced fusion reaction. A previous study reported that D614G allows more open conformation of the RBD domain of spike, which may facilitate ACE2 binding (Yurkovetskiy et al., 2020; Zhang et al., 2021). Our data suggest that D614G mutation may facilitate spike interaction with NRP1 and TMPRSS2 and promote Ca^{2+}-driven conformational rearrangement on the pathway to fusion. NRP1 is known to bind the furin-cleaved S1 domain of the SARS-CoV-2 spike proteins (Daly et al., 2020; Cantuti-Castelvetri et al., 2020). Our data suggest that D614G variants may potentiate this NRP1 interaction with S1 fragment and increase the membrane fusion efficiency. Although our experiments do not measure direct binding of spike and receptor/co-receptor (just consequences of the binding) and receptor engagement is only one interpretation, a D614G spike might be more prone to triggering as a result of binding, or the mutant spike might be more likely to engage the target membrane as a result of the same triggering.

Since no fusion events were observed at low pH even in the presence of all receptors and protease with any other

Figure 1. Ca^{2+} triggers robust SARS-CoV-2 D614G spike-mediated virus-liposome lipid mixing compared to WT spike at acidic pH

(A) Pseudovirions formed with SARS-CoV-2 WT spike or D614G spike were labeled with a self-quenching lipophilic fluorophore DiO (STAR Methods). Liposomes coated with polyhistidine-tagged hACE2 were incubated with pseudovirion followed by adjustment to the desired pH. Where indicated, 0.5 mM $CaCl_2$ was included into the reaction mixer.

(B) Fluorescence dequenching of DiO was monitored over a 20-min period at the indicated pH and presented as the fold increase over initial fluorescence (F/F_0). Dequenching was observed only in the presence of Ca^{2+} with hACE2 at pH 4.6 for both the WT (blue) and D614G spike (green). Maximal dequenching was observed for D614G (green). The data are shown as an average of four independent measurements.

(C) The degree of fusion for WT and D614G with hACE2 at pH 4.6 in presence or absence of Ca^{2+} has been normalized to fusion efficiency in the presence of 1% Triton X, which was set to 100% (Table S1).

(D) The fusion index is the extent of fusion at 20 min after the start of the fusion reaction and is plotted as indicated for conditions (n = 4 independent experiments; error bar represents standard mean). The p values by two-tailed Student's t test are indicated. p value < 0.0001 is indicated as (*), and p value < 0.00001 is indicated as (**).

(E) Pseudovirions of SARS-CoV-2 spike or D614G spike were mixed with liposomes coated with polyhistidine-tagged NRP1-b1, followed by adjustment to the desired pH, in the presence or absence of 0.5 mM $CaCl_2$ into the reaction mixer.

(F) Fluorescence dequenching was observed only in the presence of Ca^{2+} with NRP1-b1 at pH 5 and 4.6 for both the WT (blue) and D614G spike (green). The data are shown as an average of four independent measurements.

(G) D614G spike shows a high degree of fusion compared to WT in the presence of Ca^{2+} at low pH and NRP1-b1 (Table S1).

(H) The comparative fusion efficiency after 20 min of fusion reaction for WT and D614G at indicated pH and in presence or absence of Ca^{2+} (n = 4 independent experiments; error bar represents standard error of mean). The p values by two-tailed Student's t test are indicated.

(I) Lipid mixing assay between SARS-CoV-2 spike or D614G spike pseudovirions and liposomes coated with polyhistidine-tagged TMPRSS2.

(J) Increment of fluorescence over initial fluorescence (F/F_0) was observed only in the presence of Ca^{2+} at pH 5 and 4.6 for both the WT (blue) and D614G spike (green). The data are shown as an average of four independent measurements. D614G spike demonstrates higher fusion efficiency (K) and fusion index (L) compared to WT spike (Table S1). (n = 4 independent experiments; error bar represents standard error of mean). The p values by two-tailed Student's t test are indicated.

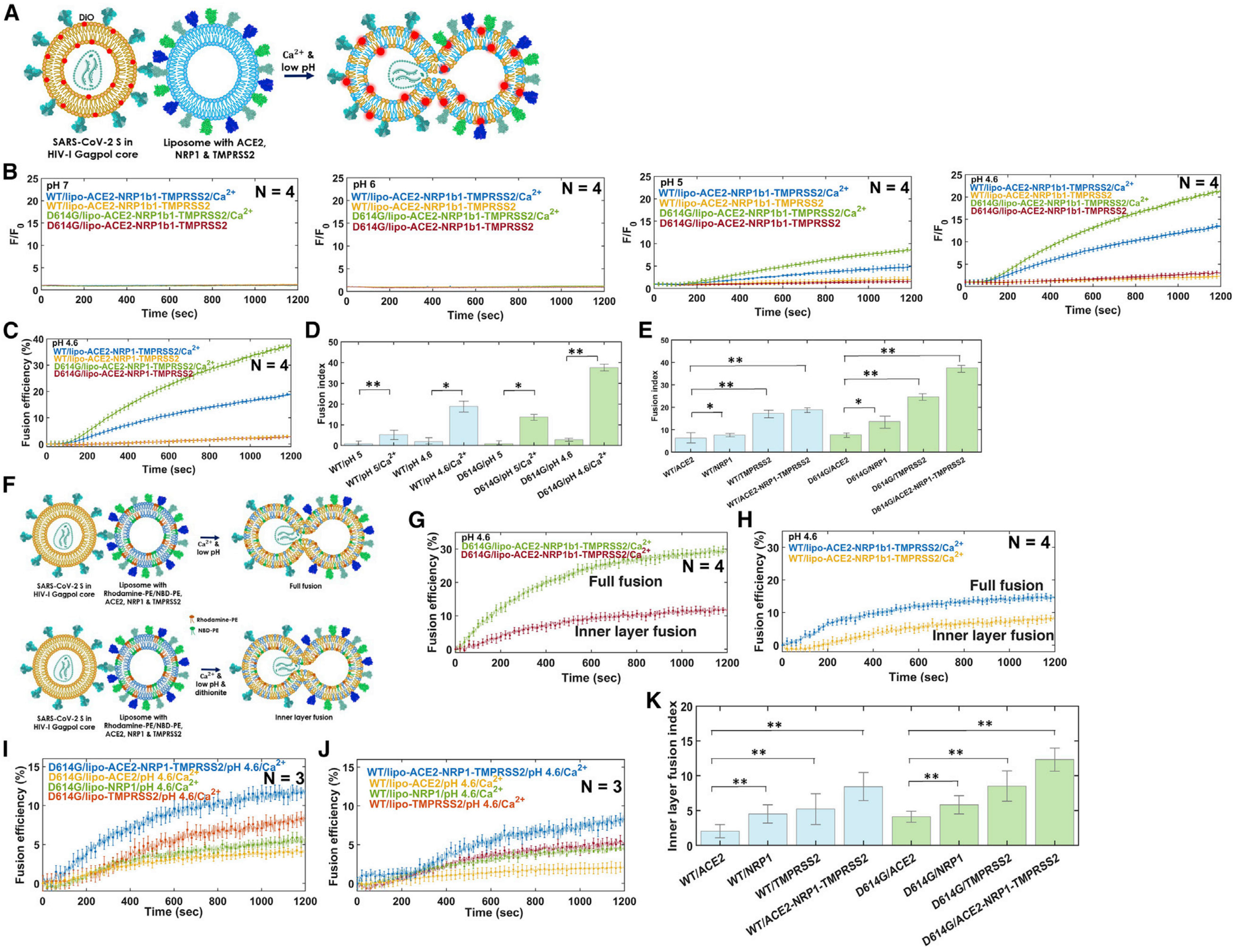

Figure 2. Ca^{2+} drives the spike-mediated full fusion between virus and liposome, and D614G is highly fusogenic

(A) DiO-labeled pseudovirions of SARS-CoV-2 spike (WT) or D614G spike were incubated with proteoliposomes and coated with polyhistidine-tagged hACE2, NRP1-b1, and TMPRSS2 at desired pH and 0.5 mM $CaCl_2$, as indicated.

(B) Fluorescence dequenching was observed only in the presence of Ca^{2+} at pH 5 and 4.6 for both the WT (blue) and D614G spike (green) in presence of all receptors (Table S1). The data are shown as an average of four independent measurements.

(C) Normalized fusion efficiency shows D614G spike virion is 2-fold fusogenic compared to the WT spike.

(D) Comparative fusion efficacy after 20 min of the fusion reaction for D614G and WT spike in presence of all receptors, at indicated pH and calcium. (n = 4 independent experiments; error bar represents standard error of mean). The p values by two-tailed Student's t test are indicated. p value < 0.0001 is indicated as (*), and p value < 0.00001 is indicated as (**).

(E) Individual receptor's role in fusion efficacy between D614G and WT in presence of low pH and 0.5 mM $CaCl_2$. (n = 4 independent experiments; error bar represents standard error of mean).

(F) FRET-based assay for probing the full fusion and inner leaflet fusion between the viral and liposomal membrane. NBD-PE (donor) and Rho-PE (acceptor) lipids were included along with other lipids in the liposome (STAR Methods). Virus and proteoliposomes were incubated at desired pH and 0.5 mM $CaCl_2$, as indicated. Inner leaflet fusion is being reported only from the dequenching of the donor dye present in the inner leaflet (STAR Methods). The full fusion and inner leaflet fusion kinetics were followed for 20 min for D614G virion (G) and WT spike virion (H) (Table S2). The data are shown as an average of three independent measurements. The comparative inner leaflet fusion efficiency in presence individual receptor ACE2, NRP1-b1, and TMPRSS2 with D614G spike virion (I) and WT spike virion (J) at pH 4.6 and 0.5 mM $CaCl_2$ (Table S2). The data are shown as an average of three independent measurements.

(K) D614G spike variant has higher inner layer fusion efficacy in any circumstance. (n = 3 independent experiments; error bar represents standard error of mean). The p values by two-tailed Student's t test are indicated.

intracellular metal ions such as Mg^{2+}, Fe^{3+}, or Zn^{2+} (Figure S3) or in the presence of Ca^{2+} chelator EDTA (Figure S2), we concluded that Ca^{2+} is an indispensable factor for SARS-CoV-2 entry.

To confirm that the lipid mixing taking place between the viral membrane and liposomal membrane is a full fusion event, we developed a FRET-based fusion assay and compared the fusion efficiency between WT spike and D614G variant (Figure 2F). We prepared liposomes with donor fluorophore-labeled lipid (NBD-PE) and acceptor fluorophore-labeled lipid (rhodamine-PE), and we coated the liposome with the recombinant ACE2,

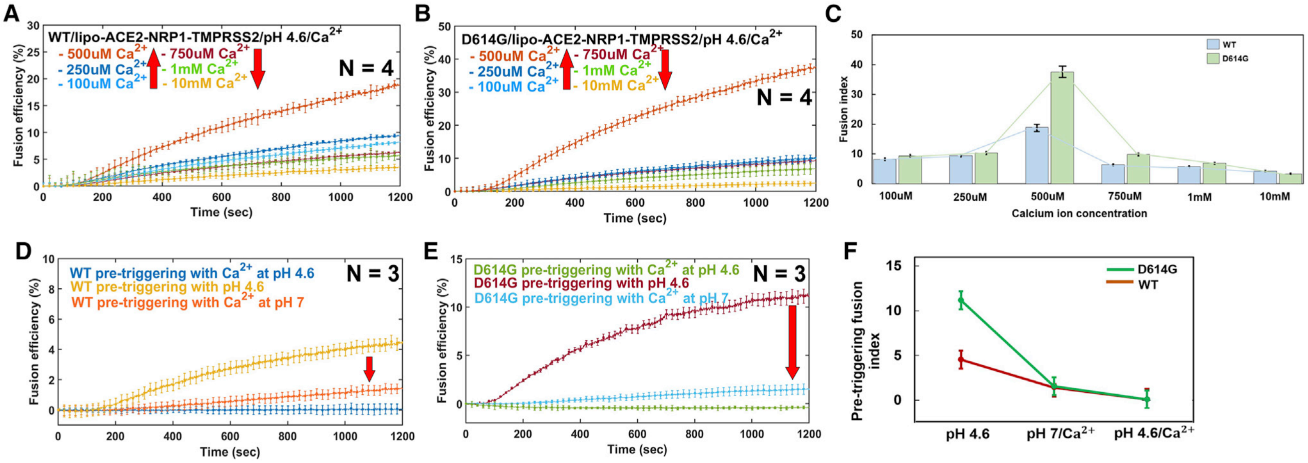

Figure 3. Dynamic Ca^{2+} concentration-dependent stimulation of D614G spike-mediated fusion

Calcium concentration-dependent fusion efficiency of WT spike virions (A) and D614G virions (B) in presence of proteoliposomes having all the receptors. Maximum fusion efficiency observed at 500 μM Ca^{2+}, where further increment of Ca^{2+} concentration decreases the fusion (Table S3). D614G spike shows pronounced calcium concentration-dependent fusion efficiency, and its fusion efficacy is almost double at 500 μM Ca^{2+} (Table S3).

(C) Fusion efficacy at varying Ca^{2+} concentration for D614G spike and WT spike reflects the high Ca^{2+} sensitivity for D614G. (n = 4 independent experiments; error bar represents standard error of mean).

(D) Pre-triggering the WT spike virions with 500 μM Ca^{2+} and pH 4.6 abrogates the fusion efficiency (blue); pre-triggering with 500 μM Ca^{2+} with neutral pH lowers the fusion efficiency (orange); pre-triggering with only low pH 4.6 does not have a significant impact on fusion efficiency (brown).

(E) Pre-triggering the D614G spike virions with low pH 4.6 (red), with 500 μM Ca^{2+} with neutral pH (cyan), and with 500 μM Ca^{2+} with low pH 4.6 (green) shows the role of calcium in pre-triggering the spike for inactivation.

(F) The fusion efficiency changes due to pre-triggering with Ca^{2+} at indicated conditions are plotted for D614G (green) and WT spike (red). (n = 3 independent experiments; error bar represents standard error of mean).

NRP1-b1, and TMPRSS2 proteins. Fusion reaction was evident for both the WT spike and D614G from seeing the increment of donor (NBD) fluorescence due to low FRET on account of fusion in the presence of low pH and calcium (Figures 2G and 2H). Fusion between the inner leaflet lipid membrane of virus and liposome is the signature of full fusion. We set out to probe the inner lipid layer fusion between the viral and liposomal membrane, where 800 μM sodium dithionite was included to quench the donor NBD dye, present on the outer leaflet of the liposomes, so the dequenching signature obtained would report the inner layer fusion (Figure 2F) (STAR Methods). Indeed, inner leaflet fusion was observed, and this demonstrates that full fusion is taking place to an extent. Consistent with the data of our DiO-based lipid mixing assay, D614G exhibited enhanced calcium-dependent full fusion and inner layer fusion in the presence of all receptors and TMPRSS2 (Figures 2G and 2H) (Figure S3). We compared the inner layer fusion efficacy in the presence of individual receptors at pH 4.6 with Ca^{2+} and found that it corroborated with lipid mixing data (Figures 2I–2K). These data confirm that the total membrane fusion, involving both the outer and the inner lipid layer fusion, is dependent on Ca^{2+} (0.5 mM) and low pH, and D614G maintained high efficacy in inner lipid layer membrane fusion compared to WT (Figure 2K).

D614G spike protein is a superior dynamic Ca^{2+} sensor to WT spike

To comprehend the nature of Ca^{2+} sensitivity of the WT spike and D614G spike, we performed the pseudovirus-liposome fusion assay at varying degree of calcium concentration, ranging from 0.1 to 10 mM. Strikingly, we found that with increments of Ca^{2+} concentration from 100 μM, the fusion efficiency increases and becomes maximum at 500 μM Ca^{2+} concentration; further increment of Ca^{2+} concentration decreases the fusion efficiency, and ultimately, fusion efficiency becomes almost marginal beyond 1 mM calcium (Figures 3A and 3B). This suggests that the spike protein is sensitive to the Ca^{2+} concentration of 500 μM, which is the physiological level of calcium at endo-/lysosomal compartment, indicating the virus entry via endo-/lysosomal route. D614G spike variant shows 2-fold more membrane fusion efficiency compared to WT at 500 μM Ca^{2+} concentration (Figure 3C). This suggests that the D614G variant has evolved to detect calcium with high sensitivity and function as a superior dynamic Ca^{2+} sensor to perform fusion reaction more efficiently compared to WT. Our data suggest that 500 μM Ca^{2+} concentration is optimum for efficient fusion, spike protein has dynamic calcium sensitivity, and D614G mutation enhances this dynamic calcium sensitivity for rapid fusion.

Pre-triggering spike with Ca^{2+} inactivates fusion

To ensure that Ca^{2+} can also pre-trigger the spike protein conformation to post-fusion state before membrane fusion, we designed a set of pre-triggering experiments. We incubated the pseudovirions (WT or D614G) with physiological Ca^{2+} concentration of 500 μM for 10 min prior to inclusion of receptor-coated liposome for fusion. We observed that pre-incubating the virus with Ca^{2+} at pH 4.6 completely abolishes the fusion (Figures 3D and 3E). Whereas pre-incubating the virus at only low pH does not affect fusion activity, addition of 500 μM Ca^{2+}

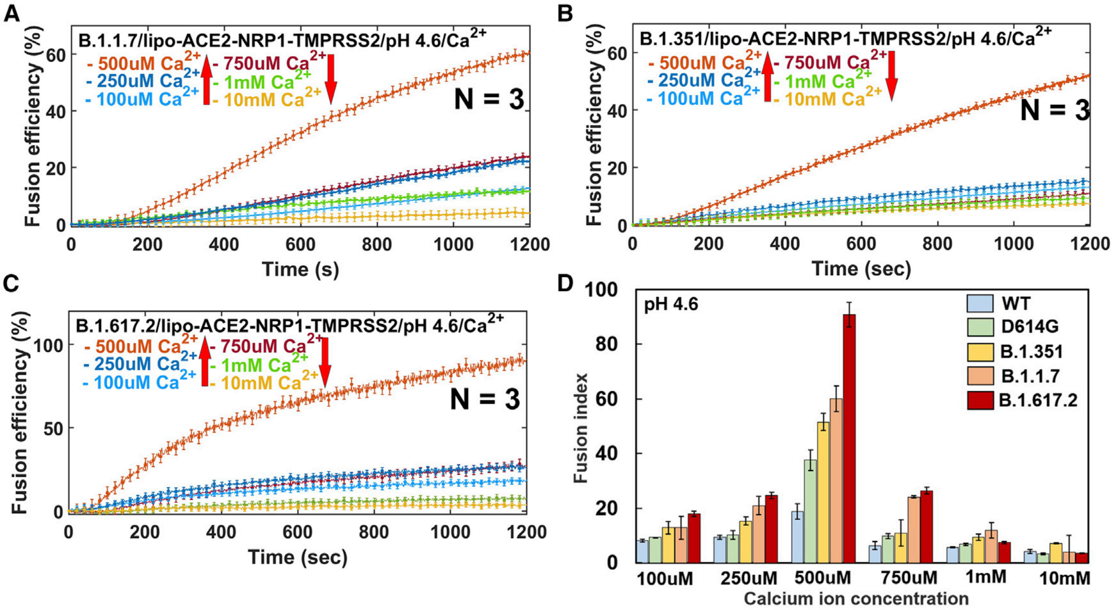

Figure 4. Dynamic Ca^{2+} sensitivity in Alpha, Beta, and Delta spike variants for membrane fusion

Calcium concentration-dependent fusion was observed for the B.1.1.7 (Alpha) variant (A), B.1. 351 (Beta) variant (B), and B.1.617.2 (Delta) spike variant (C) in DiO-based lipid mixing assay (STAR Methods). All these fusion reactions were carried out at pH 4.6 with the indicated calcium concentrations. All three strains showed highest fusion efficiency at 500 μM Ca^{2+} concentration (A, B, C). Data are shown as an average of three independent measurements, and error bar represents the standard deviation.

(D) Comparative fusion efficacy for five different strains at different calcium concentration shows that the Delta variant has the highest fusion efficacy, and the nonmonotonic nature of calcium concentration-dependence fusion is conserved across all strains. Error bars shown as standard error of mean.

restored the fusion with the same efficiency as observed for normal circumstances (Figures 3D and 3E). We find that 500 μM Ca^{2+} can even pre-trigger the spike to a significant extent even at neutral pH, and it lowers the fusion efficiency (Figure 3F). These data suggest that Ca^{2+} acts as double-edge sword: it can promote fusion and can inactivate fusion by pre-triggering the spike conformation, so spatial location of the virus and temporal dynamics of calcium are important for viral membrane fusion.

Next, to probe the role of Ca^{2+} in viral fusion inside the cell, we treated cells with a chelator of intracellular calcium, BAPTA-AM (25 μM), which abrogates both the SARS-CoV-2 spike (WT) and D614G variants' fusion and entry (Figure S1). We also performed viral fusogenecity in the presence of two potent calcium ion channel blockers, tetrandrine and verapamil, which are known to inhibit the function of two-pore calcium ion channels, TPC1 and TPC2 (Sakurai et al., 2015; Das et al., 2020). We found that both small molecules decrease the viral fusiogenicity for WT spike and D614G (Figure S4). Live cell confocal imaging data show the co-localization of pseudovirion in lysosomal compartment and co-localization of pseudovirion with TPC2 ion channel during entry (Figure S4). Collectively, our data suggest that calcium channel blocker inactivates the TPC2 and may cause Ca^{2+} accumulation inside the lysosome, which leads to Ca^{2+}-dependent pre-triggering of the spike protein conformation at low pH and fusion inactivation, as seen in our pre-triggering experiments (Figures 3D–3F).

Dynamic Ca^{2+} sensitivity with Alpha and Beta spike variants

To probe the role of Ca^{2+} in membrane fusion activities in the newly evolved spike variants, we performed the pseudovirion-liposome membrane fusion assay with B.1.1.7 and B.1.351 spike variants of concern (Figures 4A and 4B). For Alpha spike variant, we found that fusion efficiency completely depends on the calcium concentration and low pH. We performed a fusion reaction at varying degrees of calcium concentration, ranging from 0.1 to 10 mM. The B.1.1.7 spike fusion efficiency was ~15% at Ca^{2+} concentration of 100 μM, and the fusion efficiency successively increases to ~20% at 250 μM calcium concentration and becomes maximum (~60%) at 500 μM Ca^{2+} concentration (Figure 4A). Further increment of Ca^{2+} concentration to 750 μM and 1 mM decreases the fusion efficiency to ~25% and ~10%, respectively, and ultimately, fusion efficiency becomes almost marginal beyond 1 mM calcium (Figure 4A). The fusion activity of B.1.1.7 shows three times more fusion activity than Wuhan-hu-1 strain and 50% more fusion activity compared with the D614G spike. This could be due to enhanced binding of RBD of B.1.1.7 with ACE2 due to N501Y mutation, which enhances receptor recognition and fusion, or simply due to enhanced triggering, consistent with previous data (Wang et al., 2021; Zhu et al., 2021).

Like Alpha variant, we found that fusion efficiency of Beta spike variant also completely depends on the calcium concentration and low pH (Figure 4B). For B.1.351 spike variant, the fusion activity changes at varying degree of calcium concentration (0.1–10 mM). The B.1.351 spike fusion efficiency was ~15% at Ca^{2+}

concentration of 100 μM, and the fusion increases modestly to ~17% at 250 μM calcium concentration and becomes maximum (~50%) at 500 μM Ca^{2+} concentration. Further increment of Ca^{2+} concentration to 750 μM decreases the fusion efficiency to ~10%, and ultimately, fusion efficiency becomes almost marginal at Ca^{2+} concentration of 1 mM and beyond (Figure 4B). We found that Beta fusion activity is ~15% lower compared to the Alpha strain, which could be due to the lower affinity of ACE2 for B1.351 than B.1.1.7 spike variant, due to additional mutation on B.1.351 variant (K417N and E484K), consistent with a previous report (Gobeil et al., 2021). Both the Alpha and Beta spike variants evolved to be more sensitive to calcium concentration dynamics and show higher fusion activity compared to D614G and Wuhan strain, suggesting that B.1.1.7 and B.1.351 spikes facilitate calcium-based triggering for higher fusion activity.

Delta variant shows highest Ca^{2+} sensitivity for fusion

The Delta variant, B.1.617.2, has outcompeted other variants of concern to be the globally dominant strain (Mlcochova et al., 2021; Earnest et al., 2021; Dagpunar, 2020). To determine the role of Ca^{2+} in B.1.617.2 membrane fusion activity for enhanced infectivity, we performed the fusion experiments at different calcium concentration (0.1–10 mM). Like other spike strains of variants of concern, Delta variant's fusion activity showed a nonmonotonic nature of Ca^{2+} concentration dependence (Figure 4C). We found fusion efficiency of ~90% with Delta spike strains at Ca^{2+} concentration of 500 μM, which is the highest compared with other spike variants of concern (Figure 4C). Delta showed 50% and 80% more fusion activity compared to Alpha and Beta spike strains, respectively. Delta showed two and four times more fusogenicity compared to D614G and Wuhan strain, respectively (Figure 4D).

Interestingly, at low calcium concentration (100 and 250 μM) and at high concentration of calcium (750 μM or 1 mM), the difference in fusion activity among spike strains is modest, and all strains show similar fusion efficiency (Figures 4D and S5). Therefore, calcium concentration has a leveling effect in fusion activity, suggesting that optimal calcium concentration (~500 μM) is indispensable for the spike variant-dependent fusion efficiency. This suggests that the Delta variant has evolved to detect calcium with high sensitivity and function as a superior Ca^{2+} sensor to perform fusion reaction more efficiently compared with other spike strains.

Ca^{2+} accelerates fusion peptide insertion of spike S2 domain

The calcium effect on fusion activity could be due to the whole spike domain. Nonetheless, to determine the role of Ca^{2+} in fusion peptide activation of SARS-CoV-2 spike protein, we developed a fluorescence anisotropy assay to track the mobility of fusion peptide (Figure 5A). Anisotropy can determine the free state to bound state conformation change of fusion peptide during interaction with target membrane. In the context of WT spike and D614G spike, we attached Cy3 fluorophore at position 836 at the N terminus of S2, proximal to the fusion peptide, using genetic expansion code techniques (Figure S6) (Das et al., 2018; Nikić et al., 2016). To facilitate fluorophore attachment, we incorporated one ncAA at positions 836 through amber stop codon suppression (S*; Figure S6). We then produced pseudovirions with the HIV core and SARS-CoV-2 S* for WT as well as D614G S* variants. The tagged S* was then labeled with Cy3-tetrazine by Diels-Alder cycloaddition (STAR Methods). We chose this site to track the conformational changes in fusion peptide in S2 domain during translocation to the target membrane for fusion by following the anisotropy of the labeled fluorophore in real time. We find that addition of 500 μM Ca^{2+} led to a sudden increase in anisotropy, suggesting that calcium directly promotes the fusion peptide insertion to the membrane (Figure 5B). The anisotropy magnitude for D614G is significantly high, suggesting that D614G mutation facilitates fusion peptide binding to the target membrane, or alternatively the mutation allows simply greater triggering compared to WT. To understand the dynamic nature of Ca^{2+} sensitivity in fusion peptide membrane binding, we performed anisotropy measurements at different calcium concentrations for WT and D614G and found that only at 500 μM Ca^{2+} does the anisotropy increase to the maximum value, suggesting the key role of calcium concentration sensitivity on fusion peptide insertion into the membrane (Figures 5C and 5D). D614G showed 150% more efficiency for membrane binding compared to the WT spike (Figure 5E), which leads to the enhanced fusion and entry. We compared the structural features of FPPR regions between WT and D614G at pre-fusion state, and we found that D614G spike S2 fusion peptide domain is compact, and the orientation of D830 and D839 is close enough for coordinating Ca^{2+}, whereas the amino acid orientation in WT spike S2 fusion peptide domain is far less susceptible to coordinate Ca^{2+} (Figure 5F). The Ca^{2+} binding affinity of fusion peptide potentially makes the D614G fusion peptide more prone to triggering compared to WT spike (Figure 5G).

Ca^{2+} enhances pre- to post-fusion conformational change of spike S2 domain

To understand the role of Ca^{2+} on spike (S) conformation, in the presence of low pH and the recombinant receptors ACE2 and NRP1 and protease TMPRSS2, we developed a FRET-based assay that reports on the conformational changes of S protein from pre-fusion to the post-fusion state due to membrane fusion (Figure 6A), as previously developed for visualizing influenza hemagglutinin and Ebola GP conformational dynamics (Das et al., 2018, 2020). In the context of spike, we attached one fluorophore at position 836 at the N terminus of S2 at FPPR, and we attached the second fluorophore at position 1,035, adjacent to the membrane proximal region of S2 (Figure 6B). We chose these sites to track the predicted conformational changes in S2 during membrane fusion that lead to displacement of the N terminus and the fusion peptide with respect to the base of S2. Structural data suggest a significant increase in the distance (ca. 130 Å) between the fluorophores after transition from the pre-fusion to the post-fusion conformation, which we anticipated would result in high FRET to low FRET efficiency (Figure 6B). To facilitate fluorophore attachment, we incorporated two ncAAs at positions 836 and 1,035 through amber stop codon suppression (S**; Figure S6). We then formed pseudovirions with the HIV core and a SARS-CoV-2 S** for WT as well as for D614G S**. The tagged S** was then labeled with Cy3 and Cy5 by Diels-Alder cycloaddition (STAR Methods). Compared to WT S and

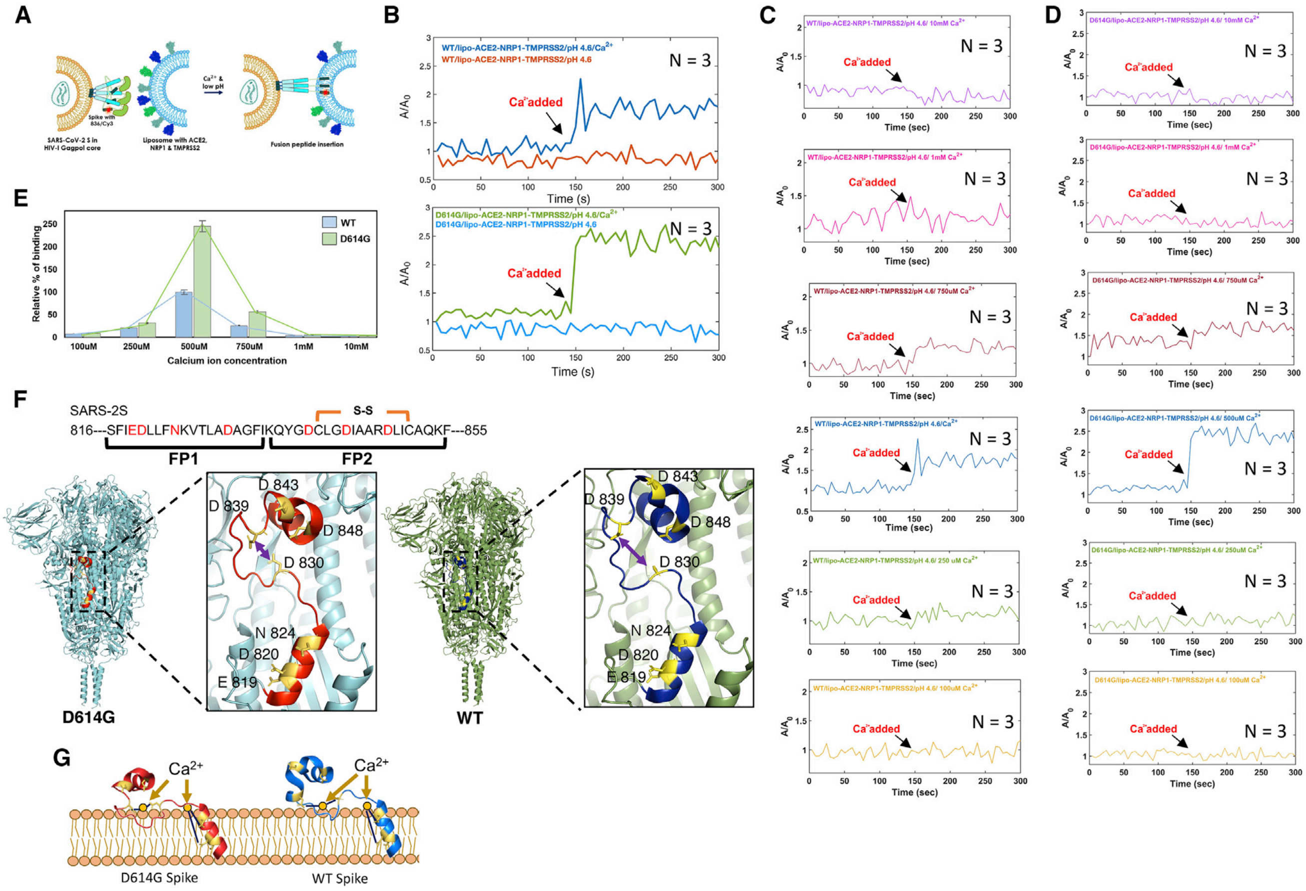

Figure 5. Ca^{2+} promotes the spike's fusion peptide for membrane penetration with high efficacy compared to WT

(A) Fluorescence anisotropy assay design for probing fusion peptide binding to target membrane by incubating pseudovirions having SARS-CoV2-S* or SARS-CoV2-D614G-S* with the proteoliposome with ACE2/NRP1/TMPRSS2 during triggering with Ca^{2+} and low pH 4.6 (STAR Methods).

(B) The change in anisotropy value in fusion peptide with time during membrane fusion in presence of Ca^{2+} and in absence of calcium at low pH 4.6 for WT and D614G spikes. The data are shown as an average of three independent measurements.

(C and D) Fluorescence anisotropy measurements were performed at different Ca^{2+} concentrations, as indicated, for both WT and D614G spikes. The point at which calcium was added (150 s) is indicated. The drastic anisotropy change indicates the binding of the fusion peptide with the membrane due to calcium stimulation, occurring only at 500 μM Ca^{2+}. The data are shown as an average of three independent measurements.

(E) The effect of Ca^{2+} concentration in anisotropy reflects the fusion peptide binding efficiency with the membrane. At 500 μM Ca^{2+}, the fusion peptide binding to membrane is maximum for both the WT and D614G, but D614G spike fusion peptide shows 150% more binding efficiency compared to WT. (n = 3 independent experiments; error bar represents standard error of mean).

(F) Amino acid sequences of the fusion loop for SARS-2S are indicated; the fusion loop is comprised of FP1 and FP2, and the acidic amino acids are highlighted (red) as the plausible Ca^{2+} binding site. Structural features of pre-fusion trimeric spike SARS-CoV-2 WT (PDB: 6XR8) and SARS-CoV-2 D614G spike (PDB: 7KRQ) and the close-up view of fusion peptide domain (S2$^{816-855}$) for SARS-CoV-2 WT spike and SARS-CoV-2 D614G spike showing the conformational difference in the loop and different orientation of side chain of D810 and D839 amino acids.

(G) Mechanistic model of fusion peptide translocation into membrane, where D614G spike variant can penetrate more into the target membrane due to efficient Ca^{2+} binding, compared to WT spike.

D614G-S, S**-Cy3/Cy5 and D614G-S**-Cy3/Cy5 maintained approximately 90% and 92% functionality in virus fusogenicity, respectively (Figures S6E and S6F). These indicate that S**-Cy3/Cy5 maintains a near-native global pre-fusion conformation reflective of WT spike. We first took the FRET emission spectra of spike-labeled pseudovirus in presence of proteoliposome at low pH only, conditions predicted to favor the pre-fusion conformation of spike (Figure 6C). Emission spectra showed high acceptor intensity, so it represents the predominant high-FRET state, indicating the pre-fusion conformation of the spike protein WT and D614G variants (Figure 6C). Addition of Ca^{2+} of 500 μM led to a major change in FRET emission spectra. The Ca^{2+} stimulation decreases the acceptor intensity and increases the donor intensity, and it showed a predominantly low-FRET state for both the WT spike and D614G spike (Figure 6C). This indicates that calcium destabilizes the pre-fusion conformation and promotes conformations in which the S2 domain N terminus has moved to positions distal to the trimer axis and forms low-FRET post-fusion conformation. To understand the calcium concentration sensitivity in conformational change, we performed FRET

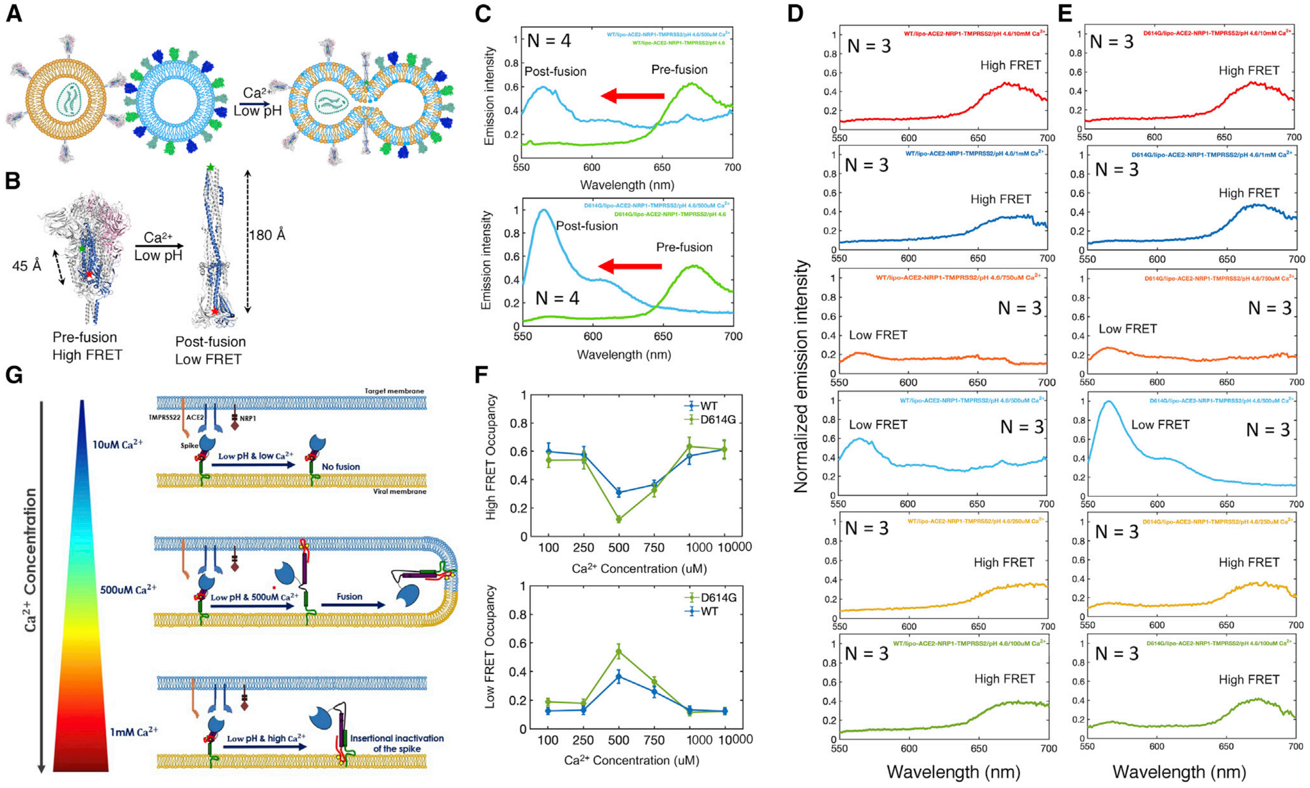

Figure 6. Ca^{2+} promotes the spike protein trimer's structural change from pre-fusion to post-fusion conformation with high efficiency during fusion

(A) Fluorescence resonance energy transfer (FRET) assay design for probing spike (S) protein conformation change from pre-fusion to post-fusion state by incubating pseudovirions having SARS-CoV2-S** or SARS-CoV2-D614G-S** with the proteoliposome with ACE2/NRP1/TMPRSS2 during triggering with Ca^{2+} and low pH 4.6 (STAR Methods).

(B) Structural model of pre-fusion spike trimer (PDB: 6XR8) and post-fusion spike trimer (PDB: 6XRA) showing the change in distance separation between the donor and acceptor fluorophores due to fusion-relevant conformational change.

(C) FRET emission spectra for WT spike and D614G spike in presence and absence of Ca^{2+} at pH 4.6. Only low pH prefers the high-FRET pre-fusion state, as observed from high acceptor intensity, and addition of Ca^{2+} triggers the conformational change to low-FRET post-fusion state, as indicated from the high donor intensity. The data are shown as an average of four independent measurements.

(D and E) The FRET emission spectra as a measure of conformational change was measured at different Ca^{2+} concentration for WT (D) and D614G spike (E). The data are shown as an average of three independent measurements.

(F) Quantification of the occupancies in the high-FRET pre-fusion and low-FRET post-fusion conformations at different at different Ca^{2+} concentration for WT spike (blue) and D614G spike (green) in the presence of liposomes, which was determined from FRET emission spectra. For D614G spike, with increment of the Ca^{2+} concentration, the population for pre-fusion conformation decreases and the population for post-fusion conformation increases more compared to WT spike. The maximum post-fusion conformation for D614G was found at 500 μm Ca^{2+} concentration. (n = 3 independent experiments; error bar represents standard error of mean).

(G) Mechanistic model of Ca^{2+}-driven activation of spike protein (shown as a protomer for simplicity) conformational change for membrane fusion.

measurements at different calcium concentrations for WT spike and D614G (Figures 6D and 6E). Remarkably, we find that only at physiological level 500 μM Ca^{2+} that both the WT and D614G spikes attain the low-FRET post-fusion state (Figures 6D and 6E), consistent with fusion efficiency data and suggesting the importance of calcium concentration for major conformational change of S2 from pre-fusion to post-fusion state. We quantified the high-FRET pre-fusion spike conformation and low-FRET post-fusion spike conformation state at varying Ca^{2+} concentrations for both WT and D614G spikes, and we found that only at ~500 μM Ca^{2+} concentration, the population for post-fusion state is maximum. This further confirms the Ca^{2+} concentration facilitates S2 conformational change for fusion. D614G showed significantly more post-fusion low-FRET population compared to WT spike (Figure 6F), which suggests that high Ca^{2+} sensitivity of D614G potentiates the pre- to post-fusion conformational change for enhanced fusion efficacy.

DISCUSSION

Our study demonstrated that SARS-CoV-2 spike is a dynamic calcium sensor, and D614G mutation and evolved spike strains B.1.1.7, B.1.351, and B.1.617.2 elicit enhanced dynamic calcium sensitivity leading to fast and efficient membrane fusion for entry. Our study provides an experimental observation of Ca^{2+}-mediated SARS-CoV-2 spike fusion peptide insertion into target membrane in the context of full-length spike protein and the structural rearrangement of spike fusion domain from prefusion state to post-fusion conformational state. While the exact site of Ca^{2+} binding to spike will be the topic of future study, our study suggests the possible interaction of Ca^{2+} with the fusion peptide in S2 domain. Sequence analysis of SARS-CoV-2 spike, as well as other viruses SARS-CoV-1-S, MERS-CoV-S, and Ebola GP, indicates universally conserved residues for binding Ca^{2+} in the fusion peptide region (E819, D820, N824, D830, D839, D843, D848) (Das et al., 2020; Lai et al., 2017; Straus et al., 2020a, 2020b). Coordinating Ca^{2+} potentially neutralizes the negative charge of these residues, triggering efficient release of the fusion peptide from the hydrophobic cleft. This charge neutralization potentially facilitates fusion peptide insertion into the target membrane, as described for the calcium-sensitive synaptotagmin, which promotes synaptic vesicle fusion (Stein et al., 2007; Südhof and Rothman, 2009).

Our results also rationalize the importance of TPC channels in SARS-CoV-2 entry, as previously observed for EBOV entry, and the inhibitory actions of calcium channel blockers (Sakurai et al., 2015; Zhang et al., 2020a, 2020b; Straus et al., 2020a, 2020b). Our results suggest that calcium channel blockers accumulate the endo-/lysosomal Ca^{2+} concentration, which may lead to premature activation of spike protein prior to fusion to target membrane (Fan et al., 2017). Therefore, the exposure of spike to Ca^{2+} must be synchronized with receptor binding and low pH to promote efficient membrane fusion (Figure 6G). Without this synchronicity, the spike may be prematurely triggered, resulting in loss of infectivity of SARS-CoV-2.

Remarkably, the WT spike, D614G, and evolved spike variants are sensitive to Ca^{2+} concentration of 500 μM for fusion, and further increment of Ca^{2+} concentration does not promote the fusion. Since the extracellular calcium concentration is in the 1–2 mM range, the spikes have evolved to only function at 500 μM Ca^{2+}, which is the physiological Ca^{2+} concentration at late endo-/lysosome (Christensen et al., 2002; Burkard et al., 2014). The Ca^{2+} concentration is relatively high in the extracellular space (~mM), but the concentration drops to $\leq$10 μM in early endosomes, due to the presence of pH-dependent Ca^{2+} channels (Gerasimenko et al., 1998; Saito et al., 2007). The Ca^{2+} concentration then begins to increase to ~0.4–0.5 mM in the late endo-/lysosome (Christensen et al., 2002). Also, D614G variant is found to be more sensitive than the WT in presence of two-pore channel (TPC) blocker tetrandrine (Figure S4). Whereas the effect of verapamil is similar for both the WT and D614G, tetrandrine is especially more potent than verapamil in blocking this TPC channel. Therefore, this difference could be due to different potency of these blockers and the high calcium sensitivity of the D614G spike.

Our results suggest a holistic model of spike-mediated membrane fusion with essential role of Ca^{2+}, receptors, and low pH (Figure 6G). Thus, in addition to the enhanced Ca^{2+} sensitivity, evolved spike protein strains seem to have Ca^{2+}-dependent enhanced nonmonotonic activity for conformational change of spike and fusion. A simple use of mM Ca^{2+} will not activate membrane-fusion activity of spike, and somewhat long incubation of virus with 500 μM Ca^{2+} at low pH inactivates the spike by pre-triggering. Our work suggests that the evolved spike proteins modulate the probability of fusion in response to the Ca^{2+} levels at lysosomal compartment, and their high dynamic Ca^{2+} sensitivity contributes to increased membrane fusion, leading to high infectivity.

Still, the membrane fusion may be possible at the plasma membrane, but the fusion rate is very slow. No fusion was observed in our reconstituted assay at neutral pH condition within the window of the first 20 min. Thus, low pH and calcium catalyze the spike-mediated membrane fusion reaction. Virus entry could happen either by plasma membrane or via late endosome pathway, but kinetics for fusion in the endo-/lysosomes path is much faster than the plasma membrane. A previous study has also reported coronavirus cellular entry occurs through the endo-/lysosomal pathway in a proteolysis-dependent manner, but the role of calcium was not delineated (Burkard et al., 2014). Our data suggest that fusion takes place through the endo-/lysosomal pathway, since the calcium ion concentration in the endosomes is around 500 μM, and the pH in the late endosomes is 4.6, making lysosome the favorable place for SARS-CoV-2 fusion and entry.

In summary, the enhanced infectivity of the Delta spike compared to Alpha, Beta, and D614G viruses largely results from the increased affinity of the spike protein to Ca^{2+}. The better exposure of RBD may facilitate the binding with all receptors, but for triggering the membrane fusion, spike fusion domain requires Ca^{2+} binding, and mutation in evolved spike strains increases the Ca^{2+} sensitivity to trigger fusion. The Delta and other evolved spike strains have gained fitness in the new host by acquiring increased calcium sensitivity for greater stability and infectivity than the parental form, indicating that high Ca^{2+} sensitivity correlates with the increased infectivity and transmissibility of the Delta strain, which has led to a greater amount of COVID-19 infection. The ability to target the Ca^{2+} binding site in spike may provide a better route for COVID-19 therapies.

Limitations of the study

Even though we have pursued a multidisciplinary approach to systematically probe the spike-mediated fusion reaction, a number of limitations remain. One of them is that the exact calcium binding residues in spike protein are not defined. In this work, we have focused on the fusion loop of S2 domain participation in the Ca^{2+}-based spike conformational triggering, but the S1 domain may also play a role in Ca^{2+}-based triggering. Another limitation is that liposome-containing receptors and protease have been used for the fusion study as a proxy of cell systems due to the technical challenge for following fusion using cell systems spectroscopically. Finally, this work has shown dynamic calcium sensitivity for different spike variants mediated fusion at reconstituted assay. Future study will reveal how calcium dynamics inside a living cell regulate virus fusion.

STAR★METHODS

Detailed methods are provided in the online version of this paper and include the following:

- KEY RESOURCE TABLE
- RESOURCE AVAILABILITY
  - ○ Lead contact

  - ○ Materials availability
  - ○ Data and code availability
- ● EXPERIMENTAL MODEL AND SUBJECT DETAILS
  - ○ Cell lines
- ● METHOD DETAILS
  - ○ Pseudotyping SARS-CoV-2 spike variants onto the HIV-1 core
  - ○ VLP production with SARS-CoV-2 spike variants
  - ○ Virus infectivity assay
  - ○ Expression and purification of recombinant hACE2, NRP1-b1 and hTMPRSS2
  - ○ Liposome preparation
  - ○ Virus-liposome lipid mixing assay
  - ○ FRET-based virus and liposome fusion assay
  - ○ Determination of inner leaflet mixing of virus and liposome
  - ○ Non-canonical amino acid incorporation into SARS-CoV-2 WT spike and D614G spike
  - ○ Fluorescent labeling of SARS-CoV-2 S^{*} and SARS-CoV-2 S^{**}
  - ○ Fluorescence anisotropy for spike membrane insertion
  - ○ FRET for spike conformational change determination
  - ○ Live-cell confocal imaging
- ● QUANTIFICATION AND STATISTICAL ANALYSIS

SUPPLEMENTAL INFORMATION

Supplemental information can be found online at https://doi.org/10.1016/j.celrep.2022.110694.

ACKNOWLEDGMENTS

The research program in the D.K.D laboratory is supported by an Intermediate Fellowship of the Wellcome Trust/DBT India Alliance (grant number IA/I/19/2/504652), the Science and Engineering Research Board (SERB) (SRG/2019/000617), and the Indian Institute of Technology, Kanpur. P.S. and S.M. are supported by Prime Minster Research Fellowship (PMRF). The authors wish to thank Jason McLellan, Stefan Pohlmann, Brett Collins, Boris Simonetti, Dr. Peter Cullen, Youxing Jiang, and Edward Lemke for sharing expression plasmids for spike variants and receptor proteins. We also thank James Munro for carefully reading our manuscripts and comments.

AUTHOR CONTRIBUTIONS

Conceptualization, D.K.D.; Methodology, P.S., S.M., S.B., and D.K.D.; Investigation, P.S., S,M., and D.K.D.; Reagents and resources, M.H., Writing - Original Draft, P.S. and D.K.D.; Writing - Review and Editing, P.S., M.H., and D.K.D.; Funding Acquisition, D.K.D.; Supervision, D.K.D.

DECLARATION OF INTEREST

The authors declare no competing interests.

Received: August 3, 2021
Revised: December 10, 2021
Accepted: March 25, 2022
Published: April 19, 2022

REFERENCES

Braga, L., Ali, H., Secco, I., Chiavacci, E., Neves, G., Goldhill, D., Penn, R., Jimenez-Guardeño, J.M., Ortega-Prieto, A.M., Bussani, R., et al. (2021). Drugs that inhibit TMEM16 proteins block SARS-CoV-2 spike-induced syncytia. Nature *594*, 88–93.

Burkard, C., Verheije, M.H., Wicht, O., van Kasteren, S.I., van Kuppeveld, F.J., Haagmans, B.L., Pelkmans, L., Rottier, P.J.M., Bosch, B.J., and de Haan, C.A.M. (2014). Coronavirus cell entry occurs through the endo-/lysosomal pathway in a proteolysis-dependent manner. PLoS Pathog. *10*, e1004502.

Cai, Y., Zhang, J., Xiao, T., Peng, H., Sterling, S.M., Walsh, R.M.J., Rawson, S., Rits-Volloch, S., and Chen, B. (2020). Distinct conformational states of SARS-CoV-2 spike protein. Science *369*, 1586–1592.

Cantuti-Castelvetri, L., Ojha, R., Pedro, L.D., Djannatian, M., Franz, J., Kuivanen, S., van der Meer, F., Kallio, K., Kaya, T., Anastasina, M., et al. (2020). Neuropilin-1 facilitates SARS-CoV-2 cell entry and infectivity. Science *370*, 856–860.

Cavrois, M., de Noronha, C., and Greene, W.C. (2002). A sensitive and specific enzyme-based assay detecting HIV-1 virion fusion in primary T lymphocytes. Nat. Biotechnol. *20*, 1151–1154.

Christensen, K.A., Myers, J.T., and Swanson, J.A. (2002). pH-dependent regulation of lysosomal calcium in macrophages. J. Cell Sci. *115*, 599–607.

Dagpunar, J. (2020). Interim estimates of increased transmissibility, growth rate, and reproduction number of the Covid-19 B.1.617.2 variant of concern in the United Kingdom. Preprint at medRxiv. https://doi.org/10.1101/2021.2006.2003.21258293.

Daly, J.L., Simonetti, B., Klein, K., Chen, K.-E., Williamson, M.K., Antón-Plágaro, C., Shoemark, D.K., Simón-Gracia, L., Bauer, M., Hollandi, R., et al. (2020). Neuropilin-1 is a host factor for SARS-CoV-2 infection. Science *370*, 861–865.

Das, D.K., Govindan, R., Nikić-Spiegel, I., Krammer, F., Lemke, E.A., and Munro, J.B. (2018). Direct visualization of the conformational dynamics of single influenza hemagglutinin trimers. Cell *174*, 926–937.e12.

Das, D.K., Bulow, U., Diehl, W.E., Durham, N.D., Senjobe, F., Chandran, K., Luban, J., and Munro, J.B. (2020). Conformational changes in the Ebola virus membrane fusion machine induced by pH , Ca^{2+}, and receptor binding. PLoS Biol. *18*, e3000626.

Dubé, M., Rey, F.A., and Kielian, M. (2014). Rubella virus: first calcium-requiring viral fusion protein. PLoS Pathog. *10*, e1004530.

Earnest, R., Uddin, R., Matluk, N., Renzette, N., Siddle, K.J., Loreth, C., Adams, G., Tomkins-Tinch, C.H., Petrone, M.E., Rothman, J.E., et al. (2021). Comparative transmissibility of SARS-CoV-2 variants delta and alpha in new England, USA. Preprint at medRxiv. https://doi.org/10.1101/2021.10.06.21264641.

Fan, H., Du, X., Zhang, J., Zheng, H., Lu, X., Wu, Q., Li, H., Wang, H., Shi, Y., Gao, G., et al. (2017). Selective inhibition of Ebola entry with selective estrogen receptor modulators by disrupting the endolysosomal calcium. Sci. Rep. *7*, 41226.

Gerasimenko, J.V., Tepikin, A.V., Petersen, O.H., and Gerasimenko, O.V. (1998). Calcium uptake via endocytosis with rapid release from acidifying endosomes. Curr. Biol. *8*, 1335–1338.

Gobeil, S.M.-C., Janowska, K., McDowell, S., Mansouri, K., Parks, R., Stalls, V., Kopp, M.F., Manne, K., Li, D., Wiehe, K., et al. (2021). Effect of natural mutations of SARS-CoV-2 on spike structure, conformation, and antigenicity. Science *373*, eabi6226.

Grabowski, F., Preibisch, G., and Gizinski, S. (2021). SARS-CoV-2 Variant of Concern 202012/01 has about twofold replicative advantage and acquires concerning mutations. Preprint at medRxiv. https://doi.org/10.1101/2020.12.28.20248906.

Hernandez, J.M., Stein, A., Behrmann, E., Riedel, D., Cypionka, A., Farsi, Z., Walla, P.J., Raunser, S., and Jahn, R. (2012). Membrane fusion intermediates via directional and full assembly of the SNARE complex. Science *336*, 1581–1584.

Hoffmann, M., Kleine-Weber, H., Schroeder, S., Krüger, N., Herrler, T., Erichsen, S., Schiergens, T.S., Herrler, G., Wu, N.-H., Nitsche, A., et al. (2020). SARS-CoV-2 cell entry depends on ACE2 and TMPRSS2 and is blocked by a clinically proven protease inhibitor. Cell *181*, 271–280.e8.

Hou, Y.J., Chiba, S., Halfmann, P., Ehre, C., Kuroda, M., Dinnon, K.H., 3rd, Leist, S.R., Schäfer, A., Nakajima, N., Takahashi, K., et al. (2020). SARS-CoV-2 D614G variant exhibits efficient replication ex vivo and transmission in vivo. Science *370*, 1464–1468.

Korber, B., Fischer, W.M., Gnanakaran, S., Yoon, H., Theiler, J., Abfalterer, W., Hengartner, N., Giorgi, E.E., Bhattacharya, T., Foley, B., et al. (2020). Tracking changes in SARS-CoV-2 Spike: evidence that D614G increases infectivity of the COVID-19 virus. Cell *182*, 812–827.e19.

Lai, A.L., Millet, J.K., Daniel, S., Freed, J.H., and Whittaker, G.R. (2017). The SARS-CoV fusion peptide forms an extended bipartite fusion platform that perturbs membrane order in a calcium-dependent manner. J. Mol. Biol. *429*, 3875–3892.

Lakowicz, J.R. (1999). Principles of Fluorescence Spectroscopy, 2ndedition (Kluwer Academic/Plenum).

Li, Q., Wu, J., Nie, J., Zhang, L., Hao, H., Liu, S., Zhao, C., Zhang, Q., Liu, H., Nie, L., et al. (2020). The impact of mutations in SARS-CoV-2 spike on viral infectivity and antigenicity. Cell *182*, 1284–1294.e9.

Mlcochova, P., Kemp, S.A., Dhar, M.S., Papa, G., Meng, B., Ferreira, I.A.T.M., Datir, R., Collier, D.A., Albecka, A., Singh, S., et al. (2021). SARS-CoV-2 B.1.617.2 delta variant replication and immune evasion. Nature *599*, 114–119.

Munro, J.B., Gorman, J., Ma, X., Zhou, Z., Arthos, J., Burton, D.R., Koff, W.C., Courter, J.R., Smith, A.B., 3rd, Kwong, P.D., et al. (2014). Conformational dynamics of single HIV-1 envelope trimers on the surface of native virions. Science *346*, 759–763.

Nathan, L., Lai, A.L., Millet, J.K., Straus, M.R., Freed, J.H., Whittaker, G.R., and Daniel, S. (2020). Calcium ions directly interact with the ebola virus fusion peptide to promote structure–function changes that enhance infection. ACS Infect. Dis. *6*, 250–260.

Nikić, I., Estrada Girona, G., Kang, J.H., Paci, G., Mikhaleva, S., Koehler, C., Shymanska, N.V., Ventura Santos, C., Spitz, D., and Lemke, E.A. (2016). Debugging eukaryotic genetic code expansion for site-specific click-PAINT super-resolution microscopy. Angew. Chem. Int. Ed. Engl. *55*, 16172–16176.

Plante, J.A., Liu, Y., Liu, J., Xia, H., Johnson, B.A., Lokugamage, K.G., Zhang, X., Muruato, A.E., Zou, J., Fontes-Garfias, C.R., et al. (2021). Spike mutation D614G alters SARS-CoV-2 fitness. Nature *592*, 116–121.

Robson, F., Khan, K.S., Le, T.K., Paris, C., Demirbag, S., Barfuss, P., Rocchi, P., and Ng, W.-L. (2020). Coronavirus RNA proofreading: molecular basis and therapeutic targeting. Mol. Cell *79*, 710–727.

Saito, M., Hanson, P.I., and Schlesinger, P. (2007). Luminal chloride-dependent activation of endosome calcium channels: patch clamp study of enlarged endosomes. J. Biol. Chem. *282*, 27327–27333.

Sakurai, Y., Kolokoltsov, A.A., Chen, C.-C., Tidwell, M.W., Bauta, W.E., Klugbauer, N., Grimm, C., Wahl-Schott, C., Biel, M., and Davey, R.A. (2015). Ebola virus. two-pore channels control Ebola virus host cell entry and are drug targets for disease treatment. Science *347*, 995–998.

Stein, A., Radhakrishnan, A., Riedel, D., Fasshauer, D., and Jahn, R. (2007). Synaptotagmin activates membrane fusion through a Ca2+-dependent trans interaction with phospholipids. Nat. Struct. Mol. Biol. *14*, 904–911.

Straus, M.R., Tang, T., Lai, A.L., Flegel, A., Bidon, M., Freed, J.H., Daniel, S., and Whittaker, G.R. (2020a). Ca(2+) ions promote fusion of middle east respiratory syndrome coronavirus with host cells and increase infectivity. J. Virol. *94*, e00426-20.

Straus, M.R., Bidon, M.K., Tang, T., Jaimes, J.A., Whittaker, G.R., and Daniel, S. (2020b). FDA approved calcium channel blockers inhibit SARS CoV 2 infectivity in epithelial lung cells. Preprint at bioRxiv. https://doi.org/10.1101/2020.07.21.214577.

Südhof, T.C., and Rothman, J.E. (2009). Membrane fusion: grappling with SNARE and SM proteins. Science *323*, 474–477.

Tegally, H., Wilkinson, E., Giovanetti, M., Iranzadeh, A., Fonseca, V., Giandhari, J., Doolabh, D., Pillay, S., San, E.J., Msomi, N., et al. (2020). Emergence and rapid spread of a new severe acute respiratory syndrome-related coronavirus 2 (SARS-CoV-2) lineage with multiple spike mutations in South Africa. Preprint at medRxiv. https://doi.org/10.1101/2020.12.21.20248640.

Volz, E., Hill, V., McCrone, J.T., Price, A., Jorgensen, D., O'Toole, Á., Southgate, J., Johnson, R., Jackson, B., Nascimento, F.F., et al. (2021). Evaluating the effects of SARS-CoV-2 spike mutation D614G on transmissibility and pathogenicity. Cell *184*, 64–75.e11.

Walls, A.C., Park, Y.-J., Tortorici, M.A., Wall, A., McGuire, A.T., and Veesler, D. (2020). Structure, function, and antigenicity of the SARS-CoV-2 spike glycoprotein. Cell *181*, 281–292.e6.

Wang, P., Nair, M.S., Liu, L., Iketani, S., Luo, Y., Guo, Y., Wang, M., Yu, J., Zhang, B., Kwong, P.D., et al. (2021). Antibody resistance of SARS-CoV-2 variants B.1.351 and B.1.1.7. Nature *593*, 130–135.

Wibmer, C.K., Ayres, F., Hermanus, T., Madzivhandila, M., Kgagudi, P., Oosthuysen, B., Lambson, B.E., de Oliveira, T., Vermeulen, M., van der Berg, K., et al. (2021). SARS-CoV-2 501Y.V2 escapes neutralization by South African COVID-19 donor plasma. Nat. Med. *27*, 622–625.

Wrapp, D., Wang, N., Corbett, K.S., Goldsmith, J.A., Hsieh, C.-L., Abiona, O., Graham, B.S., and McLellan, J.S. (2020). Cryo-EM structure of the 2019-nCoV spike in the prefusion conformation. Science *367*, 1260–1263.

Xiong, X., Qu, K., Ciazynska, K.A., Hosmillo, M., Carter, A.P., Ebrahimi, S., Ke, Z., Scheres, S.H.W., Bergamaschi, L., Grice, G.L., et al. (2020). A thermostable, closed SARS-CoV-2 spike protein trimer. Nat. Struct. Mol. Biol. *27*, 934–941.

Yurkovetskiy, L., Wang, X., Pascal, K.E., Tomkins-Tinch, C., Nyalile, T.P., Wang, Y., Baum, A., Diehl, W.E., Dauphin, A., Carbone, C., et al. (2020). Structural and functional analysis of the D614G SARS-CoV-2 spike protein variant. Cell *183*, 739–751.e8.

Zhang, L., Jackson, C.B., Mou, H., Ojha, A., Peng, H., Quinlan, B.D., Rangarajan, E.S., Pan, A., Vanderheiden, A., Suthar, M.S., et al. (2020a). SARS-CoV-2 spike-protein D614G mutation increases virion spike density and infectivity. Nat. Commun. *11*, 6013.

Zhang, L.-K., Sun, Y., Zeng, H., Wang, Q., Jiang, X., Shang, W.-J., Wu, Y., Li, S., Zhang, Y.-L., Hao, Z.-N., et al. (2020b). Calcium channel blocker amlodipine besylate therapy is associated with reduced case fatality rate of COVID-19 patients with hypertension. Cell Discov. *6*, 96.

Zhang, J., Cai, Y., Xiao, T., Lu, J., Peng, H., Sterling, S.M., Walsh, R.M.J., Rits-Volloch, S., Zhu, H., Woosley, A.N., et al. (2021). Structural impact on SARS-CoV-2 spike protein by D614G substitution. Science *372*, 525–530.

Zhou, P., Yang, X.-L., Wang, X.-G., Hu, B., Zhang, L., Zhang, W., Si, H.-R., Zhu, Y., Li, B., Huang, C.-L., et al. (2020a). A pneumonia outbreak associated with a new coronavirus of probable bat origin. Nature *579*, 270–273.

Zhou, T., Tsybovsky, Y., Gorman, J., Rapp, M., Cerutti, G., Chuang, G.-Y., Katsamba, P.S., Sampson, J.M., Schön, A., Bimela, J., et al. (2020b). Cryo-EM structures of SARS-CoV-2 spike without and with ACE2 reveal a pH-dependent switch to mediate endosomal positioning of receptor-binding domains. Cell Host Microbe *28*, 867–879.e5.

Zhu, X., Mannar, D., Srivastava, S.S., Berezuk, A.M., Demers, J.-P., Saville, J.W., Leopold, K., Li, W., Dimitrov, D.S., Tuttle, K.S., et al. (2021). Cryo-electron microscopy structures of the N501Y SARS-CoV-2 spike protein in complex with ACE2 and 2 potent neutralizing antibodies. PLoS Biol. *19*, e3001237.

STAR★METHODS

KEY RESOURCE TABLE

REAGENT or RESOURCE	SOURCE	IDENTIFIER
Antibodies		
SARS-CoV-2 RBD Rabbit PAb	Sino Biological	Cat# 40592-T62; RRID: AB_2857935
Anti-HIV p24 Rabbit PAb	Invitrogen	Cat# PA81773; RRID: AB_2788949
Mouse anti-rabbit IgG, HRP conjugated	Invitrogen	Cat# 31464; RRID: AB_228378
Chemicals, peptides, and recombinant proteins		
DOPC	Avanti Polar Lipids	Cat# 850375P
POPC	Avanti Polar Lipids	Cat# 850457
Brain PS	Avanti Polar Lipids	Cat# 840032C
DSPE-PEG Biotin	Avanti Polar Lipids	Cat# 880129P
Cholesterol	Avanti Polar Lipids	Cat# LM4100
Liss-Rhodamine-PE	Avanti Polar Lipids	Cat# 810150C
NBD-PE	Avanti Polar Lipids	Cat# 810145P
trans-cyclooct-2-ene ncAA (TCO*)	Si-Chem	Cat# SC-8008
Cy5-tetrazine	Jena Bioscience	Cat# CLK-015-05
Cy3-tetrazine	Jena Bioscience	Cat# CLK-014-05
DiO	Invitrogen	Cat# V22886
DiD	Invitrogen	Cat# D7757
LysoTracker DeepRed	Invitrogen	Cat# L12492
DMEM	GIBCO	Cat# 11995065
Trypsin	GIBCO	Cat# 253000-054
L-glutamine	GIBCO	Cat# 25030-081
Fetal Bovine Serum	GIBCO	Cat# A3160802
OptiMEM	GIBCO	Cat# 31985-070
Penicillin-Streptomycin	GIBCO	Cat# 15140-122
HBSS	GIBCO	Cat# 14025-092
Phenol Red-free DMEM	GIBCO	Cat# 21063-029
Lipofectamine	Invitrogen	Cat# 100022052
Opti-Prep	Sigma	Cat# D1556
Triton X-100	Sigma	Cat# 9036195
SuperSignal West Pico	Thermo Fisher	Cat# 34577
BAPTA-AM	Sigma	Cat# A1076
Tetrandrine	Sigma Aldrich	Cat #Y001165
Verapamil hydrochloride	Sigma Aldrich	Cat# V4629
Polyethyleneimine (PEI)	Poly Sciences	Cat# 23966
Ni-Sepharose beads	GE Healthcare	Cat# 17531801
Critical commercial assays		
Q5 Site-Directed mutagenesis kit	NEB	Cat# E0554S
LiveBLAzer FRET-B/G Loading Kit with CCF4-AM	Invitrogen	Cat# K1085
Experimental models: Cell lines		
HEK293T/17	ATCC	Cat# CRL-11268
FreeStyle 293F	Thermo Fisher	Cat# R79007
Recombinant DNA		
Plasmid encoding HIV-1 Gag-Pol	Yale University (Mothes laboratory)	N/A
Plasmid encoding VSV-G	Tufts University (Coffin laboratory)	N/A

(*Continued on next page*)

Continued

REAGENT or RESOURCE	SOURCE	IDENTIFIER
Plasmid encoding SARS-CoV-2 wild type Spike	GenScript	N/A
Plasmid encoding SARS-CoV-2 D614G Spike	This paper	N/A
Plasmid encoding SARS-CoV-2 B.1.1.7 Spike	David Ho	N/A
Plasmid encoding SARS-CoV-2 B.1.351 Spike	David Ho	N/A
Plasmid encoding SARS-CoV-2 B.1.617.2 Spike	Stefan Pohlmann	N/A
Plasmid encoding full-length ACE2	Stefan Pohlmann	N/A
Plasmid encoding ACE2 ectodomain	This paper	N/A
Plasmid encoding full-length TMPRSS2	Stefan Pohlmann	N/A
Plasmid encoding TMPRSS2 ectodomain	This paper	N/A
Plasmid encoding full-length NRP1	Boris Simonetti	N/A
Plasmid encoding NRP1-b1	Brett Collins	N/A
SARS-CoV-2 WT $^{836\ \mathrm{TAG}}$ (S*)	This paper	N/A
SARS-CoV-2 D614G $^{836\ \mathrm{TAG}}$ (S*)	This paper	N/A
SARS-CoV-2 WT $^{836\mathrm{TAG}/1035\mathrm{TAG}}$ (S**)	This paper	N/A
SARS-CoV-2 D64G $^{836\mathrm{TAG}/1035\mathrm{TAG}}$ (S**)	This paper	N/A
Plasmid encoding eRF1 with E55D mutation	Edward Lemke	N/A
Plasmid encoding TPC1-GFP	Youxing Jiang	N/A
Plasmid encoding TPC2-GFP	Youxing Jiang	N/A
Plasmid encoding SARS-CoV-2 Membrane protein	AddGene	Cat# 141386
Plasmid encoding SARS-CoV-2 Nucleocapsid protein	AddGene	Cat# 141391
Plasmid encoding SARS-CoV-2 Envelope protein	AddGene	Cat# 141385
Plasmids encoding NESPylRSAF/tRNAPyl	Nikić et al., 2016	N/A
Plasmid encoding BlaM-Vpr	Cavrois et al., 2002	AddGene, Cat# 21950
Software and algorithms		
Zen 3.4 (Blue Edition)	Carl Zeiss	N/A
MATLAB	Mathworks	N/A
Felix Gx	HORIBA Scientific	N/A
ImageJ	NIH	N/A
PyMol	Schrodinger	N/A

RESOURCE AVAILABILITY

Lead contact

Further information and requests for resources and reagents should be directed to the Lead Contact, Dibyendu Kumar Das (dkdas@iitk.ac.in).

Materials availability

All the reagents and plasmids generated in this study will be shared upon request to the lead contact.

Data and code availability

- Data generated in this study will be shared upon request to the lead contact.
- This paper does not report original code.
- Any additional information to reanalyse the data reported in this paper is available from the lead contact upon request.

EXPERIMENTAL MODEL AND SUBJECT DETAILS

Cell lines

HEK293T/17 cells were obtained from ATCC and were maintained in DMEM (GIBCO) supplemented with 10% fetal bovine serum (GIBCO) and 100 U/mL penicillin-streptomycin (GIBCO). HEK293T/17 cell lines were maintained at 37°C, 5% CO_2. Freestyle 293-F cells were from ThermoFisher and were maintained as per the manufacturer's guidelines. Freestyle 293-F cell lines were maintained at 37°C, 8% CO_2.

METHOD DETAILS

Pseudotyping SARS-CoV-2 spike variants onto the HIV-1 core

HEK293T/17 cells were transfected with plasmids encoding HIV-1 GagPol and either wild type SARS-CoV-2 spike (Wuhan) or SARS-CoV-2 D614G/B.1.1.7/B.1.351/B.1.617.2 spike variant. HEK293T/17 cells were maintained in DMEM (GIBCO), supplemented with 10% FBS (GIBCO), 2mM L-glutamine (GIBCO) and 100U/mL penicillin/streptomycin (GIBCO) at 37°C, with 5% CO_2. Cells were co-transfected with lipofectamine (Invitrogen) at 60–75% confluency. Viruses were harvested at 72 h post-transfection and were filtered through a 0.45um filter to remove cell debris. The filtered viruses were then concentrated in a 10% sucrose cushion by centrifugation at 25,000xg for 2 h. Expression of the pseudoviral particles was checked by Western blot as being positive for spike and HIV-1 p24 expression (Figure S1A).

VLP production with SARS-CoV-2 spike variants

S-MEN coronavirus like particles were produced with SARS-CoV-2 spikes incorporated in the surface of viral particle. To generate S-MEN particles, plasmids encoding pCMV-S (Wuhan/D614G/B.1.1.7/B.1.351/B.1.617.2 variant), pLVX-M (SARS-CoV-2 membrane protein plasmid), an pLVX-E (SARS-CoV-2 envelope protein plasmid, and pLVX-N (SARS-CoV-2 nucleocapsid expressing plasmid) were transfected at a ratio of 5:5:5:5 into HEK293T/17 cell. pLVX plasmids are gifts from Nevan Krogan, UCSF. S-MEN particles carrying S proteins were harvested 48 h post-transfection, filtered through syringe filter with 0.45 mm pore size, and sedimented through a 10% sucrose cushion at 25,000 rpm for 2 h. The virus pellets were then re-suspended in 50 mM pH 7.5 HEPES buffer supplied with PBS buffer.

Virus infectivity assay

The fusogenicity of the pseudotyped virions was tested by a β-lactamase (BlaM)-based enzymatic assay (LiveBlazer FRET B/G kit, Invitrogen) (Cavrois et al., 2002). The pseudoviruses were formed as described above, but with an additional plasmid encoding BlaM, fused to the HIV-1 Vpr protein. Viruses were collected and concentrated as described above and resuspended in phenol red-free DMEM (GIBCO), supplemented with 10% FBS (GIBCO), 2mM L-glutamine (GIBCO) and 100U/mL penicillin/streptomycin (GIBCO). HEK293T/17 cells, transfected individually with full-length ACE2, NRP1 and TMPRSS2 expression plasmids or in combination with all ACE2/NRP1/TMPRSS2 were seeded in 96 well plates and incubated in ice for few minutes. The virions were then used for infecting HEK293T/17 cells. Spinoculation was done at 3700 rpm at 4°C. Unbound viruses were removed by washing with HBSS (GIBCO) and resuspending the cells in fresh phenol red-free DMEM. The plate was then incubated at 37°C for 90 min to permit viral entry. Cells were then loaded with the substrate, CCF4-AM fluorophore, in presence of probenecid at a final concentration of 2.5mM. The plate was incubated overnight at 11°C. The cleavage of CCF4-AM by BlaM was detected using a plate reader (Biotek). Virus particle with D614G spike shows approximately double fusiogenicity compared to WT spike (Figure S1B). Alternatively, to probe the role of calcium in viral entry, HEK293T/17 cells were treated with intracellular calcium chelator BAPTA-AM before virus infection. Sequestering intracellular Ca^{2+} completely abrogate the viral entry for both the WT and D614G spike pseudovirions (Figure S1B). The fusogenicity of the virus was calculated as a ratio of blue to green emission. VSV-G was used as a positive control and viruses with only HIV-Gagpol were used as negative control.

Expression and purification of recombinant hACE2, NRP1-b1 and hTMPRSS2

Human ACE2 (1-615aa) with C-terminal polyhistidine and human TMPRSS2 (1-492aa) with C-terminal polyhistidine were expressed in FreeStyle 293F cells (ThermoFisher) with polyethyleneimine (PEI; Sigma-Aldrich). Six days post transfection, the supernatant containing the secreted protein was harvested and syringe-filtered using a 0.45um filter. The filtered supernatant was then incubated with Ni-Sepharose beads (GE healthcare) for 2 h for binding. The beads bound with hACE2 or hTMPRSS2 were then washed and the protein was eluted with 20 mM Tris, 250 mM imidazole, 300 mM NaCl, and buffer were exchanged into 20 mM Tris- HCl, 100 mM NaCl, 2 mM b-mercaptoethanol and 15% glycerol, followed by concentration with Vivaspin 6 spin filters (Sartorius). The purified hACE2 and hTMPRSS2 were stored at −80°C until use.

NRP1-b1(273-427aa) with N terminal polyhistidine was expressed in BL21Star^{TM}-(DE3) cells (Invitrogen). Cells were grown at 37°C, and once the cells reached an O.D. value of 0.6, induction was done with 750uM isopropyl β-D-1-thiogalactopyranoside (IPTG) (Sigma). After induction, cells were grown at 22°C for 16 h, following which, they were harvested, centrifuged, lysed and purified using Ni-Sepharose fast flow beads as per stander means described above.

Liposome preparation

Liposomes were prepared in a 4:4:0.5:0.1:2 ratio of 1,2, dioleoyl-sn-glycero-3-phosphocholine (DOPC; Avanti Polar Lipids), 1-palmitoyl-2-oleoyl-glycero-3-phosphocholine (POPC; Avanti Polar Lipids), phosphatidylserine (PS; Avanti Polar Lipids), Ni-NTA DGS lipid (Avanti Polar Lipids) and cholesterol (Avanti Polar Lipids), as per previously described protocol (Das et al., 2020). Briefly, the lipids were mixed in chloroform, which was evaporated under a stream of argon gas. The dried lipid film was resuspended in HNE buffer (5mM HEPES, 145mM NaCl; pH 7.5), which was followed by five freeze-thaw cycles. Liposomes were obtained by extruding the homogenized aqueous lipid suspension through a polycarbonate membrane filter with pore sizes of 100nm. In order to coat the liposomes with proteins, liposomes were incubated with Histidine-tagged protein(s) of interest at 37°C for at least 1 h in rotation.

Recombinant hACE2, NRP1-b1 and hTMPRSS2, when coated together with the liposome were used in a stoichiometry of 1:1:1 in excess of liposome.

Liposomes for FRET-based fusion assay were prepared in a 4:4:0.5:0.1:2:0.1:0.1 ratio of 1,2,dioleoyl-sn-glycero-3-phosphocholine (DOPC; Avanti Polar Lipids), 1-palmitoyl-2-oleoyl-glycero-3-phosphocholine (POPC; Avanti Polar Lipids), phosphatidylserine (PS; Avanti Polar Lipids), Ni-NTA DGS lipid (Avanti Polar Lipids), cholesterol (Avanti Polar Lipids), 1,2-dioleoyl-*sn*-glycero-3-phosphoethanolamine-N-(lissamine rhodamine B sulfonyl) (Rhod PE; Avanti Polar Lipids) and 1,2-dipalmitoyl-*sn*-glycero-3-phosphoethanolamine-N-(7-nitro-2-1,3-benzoxadiazol-4-yl) (NBD PE; Avanti Polar Lipids). The procedure for liposome preparation for FRET was same as described above. Polyhistidine tagged recombinant hACE2, NRP1-b1 and hTMPRSS2, were incubated together with the liposome were used in a stoichiometry of 1:1:1.

Virus-liposome lipid mixing assay

The viral membrane of virions with either WT spike or D614G spike were incubated with 20uM DiO for 2 h at room temperature. The labeled virions were then purified on a 6%–30% Opti-Prep (Sigma-Aldrich) gradient ultracentrifugation at 35,000 rpm for 1 h. The fractions having the labeled virus were collected and used for the virus-liposome fusion assay. DiO-labelled virions with either WT spike or D614G spike were combined with proteo-liposomes coated with either hACE2-ectodomain or NRP1-b1 or hTMPRSS2-ectodomain or all the receptor together and incubated for 5 min to enable virus and liposome binding at pH 7. Buffer solution was added by stopped-flow manner to adjust desired pH conditions and DiO fluorescence was followed in time-based manner. To measure the role of Ca^{2+} on fusion, $CaCl_2$ was added to the respective pH solution at the desired concentration. For time-based measurement of DiO fluorescence, DiO was excited at 488 nm and fluorescence was detected at 515 nm at every second's intervals for 20 min in a QuantaMaster fluorescenc spetrometer 8450 (Horiba). All the fusion experiments were performed at 37C by rapid peltier temperature-controlled sample holder. Data was acquired with the software provided by the manufacturer. All dequenching data acquired related to fusion were fitted to the exponential function A (1- exp-(kt^n)) (Tables S1–S4).

FRET-based virus and liposome fusion assay

Virus-liposome membrane fusion was monitored by using liposomes having the lipid conjugated FRET pair Rhodamine (RHO) and Nitrobenzoxadiazole (NBD) (Hernandez et al., 2012). Virions having wither WT spike or D614G spike were mixed with NBD/RHO-labeled liposomes, coated with recombinant hACE2, NRP1-b1 and hTMPRSS2, maintaining equal stoichiometry (1:1:1). Liposome fusion reactions were performed and measured in a Quantamaster spectrometer (Model-QM8450) equipped with a magnetic stirrer and a temperature controller (Horiba). Data was acquired with the FelixGx software provided by the manufacturer. Excitation and emission wavelengths were 460 nm and 538 nm, respectively, and all the reactions were performed at 37°C. The reactions were started by mixing virions and proteo-liposomes (20–25 μL each) in buffer solution with desired pH in presence of $CaCl_2$ (0.5mM) and after monitoring the fusion for 20 min the reaction was terminated by adding Triton X-100 (Sigma, 0.01% (v/v)). Full fusion was measured as a function of NBD dequenching signal due to fusion. Dequenching signals were normalized to the maximum fluorescence produced by detergent solubilization and fusion curves were plotted as a percentage of the fusion efficiency, considering the maximum fusion efficiency with 0.01% Triton X-100 as 100%.

The following expression denotes the percentage of fusion efficiency:

$$(F_t - F_0)/_{F_\infty - F_0} * 100$$

Here, F_∞ denotes the maximum fluorescence intensity obtained by detergent solubilization. All donor dequenching data acquired related to fusion were fitted to the exponential function A(1- exp-(kt^n)) (Tables S2 and S3).

Determination of inner leaflet mixing of virus and liposome

Inner leaflet fusion, or inner fusion is defined as fusion being reported only from the dequenching of the dye present in the inner leaflet. In order to quench all the dye molecules present on the outer leaflet, NBD/Rho-PE-coated liposomes coated with the proteins (ACE2, NRP1 or/and TMPRSS2) incubated for 5 min with 800uM sodium dithionite at room temperature, after which unlabelled pseudovirions were added, followed by addition of the triggering solution and measurement of the fusion activity in terms of dequenching of the dye.

To monitor the inner lipid membrane fusion between the virion and liposome, sodium dithionite was used at a concentration of 800 uM to quench the NBD fluorescence present at the outer leaflet of the NBD-PE/RHO-PE labeled liposomes (Hernandez et al., 2012). Liposomes were incubated with dithionite for 30 min, and following dithionite reduction, virions having either WT spike or D614G spike were mixed, and inner leaflet lipid-mixing were measured exactly as described for total lipid-mixing earlier. All measurements were carried out at 37°C.

To compare total and inner leaflet lipid-mixing traces, the measured inner leaflet lipid-mixing (F_{in}) was normalized to the maximum fluorescence obtained by detergent solubilization of the total lipid-mixing trace (F_{max}) according to the expression:

$$(F_{in} - F_{in0})/_{F_{max} - F_{in0}} * 100$$

Where, F_{in0} is the inner leaflet fluorescence at initial time (t_0).

Non-canonical amino acid incorporation into SARS-CoV-2 WT spike and D614G spike

We incorporated two TCO* ncAAs into the S2 domain of SARS-CoV-2 WT spike and D614G spike through amber stop codon suppression, as previously done for influenza HA and Ebola GP (Das et al., 2018, 2020). To this end, we introduced TAG codons at position 836 of S2 near the fusion peptide proximal residue (FPPR), and at position 1035 by site-directed mutagenesis. Translation proceeds through the UAG codons on the mRNA only in the presence of an orthogonal tRNA (tRNA^{Pyl}), which recognizes the UAG codon, and a corresponding aminoacyl-tRNA synthetase (NESPylRS^{AF}). NESPylRS^{AF} aminoacylates the suppressor tRNA with TCO*, facilitating its incorporation at specific locations into S, forming S**. The efficiency of amber suppression is limited due to competition of the eukaryotic release factor 1 (eRF1) with tRNA^{Pyl}. Expression of the dominant negative eRF1 E55D mutant increased amber suppression efficiency.

The formation of SARS-CoV-2 spike pseudotyped virion was first evaluated by transfecting HEK293T cells with plasmids encoding the Spike, TAG-mutated S and NESPylRS^{AF}/tRNA^{Pyl}, eRF1 E55D, and HIV-1 Gag-Pol. The growth medium was supplemented with 0.5 mM TCO* ncAA (SiChem). At 72 h post-transfection the virus was harvested, concentrated by centrifugation and evaluated by fusion assay (Figure S6). Similarly SARS-CoV-2 D614G spike pseudotyped virion was first evaluated by transfecting HEK293T cells with plasmids encoding the D614G Spike, TAG-mutated D614G-S and NESPylRS^{AF}/tRNA^{Pyl}, eRF1 E55D, and HIV-1 Gag-Pol.

Fluorescent labeling of SARS-CoV-2 S* and SARS-CoV-2 S**

For anisotropy and FRET measurements, virions were formed with on average a single S* or S** protomer among the distribution of wild-type S, as has been done previously for smFRET imaging studies of influenza hemagglutinin, Ebola GP and HIV-1 Env (Das et al., 2018, 2020; Munro et al., 2014). For anisotropy measurements, HEK293T/17 cells were transfected with a 1:5 ratio of plasmids encoding SARS-CoV-2S* and wild-type SARS-CoV-2S, and plasmids encoding HIV-1 Gag-Pol, NESPylRS^{AF}/tRNA^{Pyl}, and eRF1 (E55D), and grown in the presence of 0.5 mM TCO* ncAA. Virus was harvested, concentrated by centrifugation, and resuspended in phosphate buffer pH 7.5. Virions were then labeled by incubation with 2 mM 3-(p-benzylamino)-1,2,4,5-tetrazine-Cy3 for 10 min at 37°C. Labeled virions were purified from unbound dye using 6–30% OptiPrep gradient by ultracentrifugation at 35,000 rpm for 1 h in 50 mM Tris pH 7.4, 100 mM NaCl. The gradient was fractionated, and the fractions containing virus were identified by p24 Western blot. Similarly, Cy3 labeled D614G-S* virions were produced. The purified fluorescently labeled virus was stored at −80°C until use in anisotropy experiments.

For FRET measurements, HEK293T/17 cells were transfected with a 1:5 ratio of plasmids encoding SARS CoV-2S** and wild-type SARS-CoV-2S, and plasmids encoding HIV-1 Gag-Pol, NESPylRS^{AF}/tRNA^{Pyl}, and eRF1 (E55D), and grown in the presence of 0.5 mM TCO* ncAA. After harvesting, concentrating by centrifugation, and resuspending in phosphate buffer pH 7.5. Virions were then labeled by incubation with 2 mM 3-(p-benzylamino)-1,2,4,5-tetrazine-Cy3 and 2 mM 3-(p-benzylamino)-1,2,4,5-tetrazine-Cy5 for 10 min at 37°C. Cy3/Cy5 labeled D614G-S** virions were produced following similar procedure. The purified labeled virus was stored at −80°C until use in FRET experiments.

Since, our sample is not a soluble protein but rather a labeled virion, precise determination of labeling efficiency is not readily accomplished. The standard method does not apply since there is no way to convert the absorbance of a virion to the concentration of the envelope glycoprotein specifically. The best we can say is that the reported efficiencies of copper-free click labeling to the TCO* amino acid are in the range of 90% using 1.5μM fluorophore-tetrazine incubated for 10 min at 37°C temperature (Nikić et al., 2016; Das et al., 2020). In our labeling reactions, since we were not limited by the toxicity of the fluorophore, virions containing S* or S** were labeled using 2mM fluorophore-tetrazine for 10min at 37C. We are therefore confident that our labeling efficiency is at least as high as previously reported numbers; no labeling was observed in the absence of S* or S**.

We performed fusiogenicity measurements with pseudovirions containing either 100% wild-type Spike, 100% S*-Cy3, or 100% S**-Cy3/Cy5. The WT-S*-Cy3 and WT-S**-Cy3/Cy5 has been found to be 92% and 90% fusogenic relative to WT-S respectively and D614G-S*-Cy3 and D614G-S**-Cy3/Cy5 is 95% and 92% fusogenic relative to D614G spike respectively (Figure S6).

Fluorescence anisotropy for spike membrane insertion

Fluorescence anisotropy from a fluorophore measures the polarization of emission when the fluorophore is excited with polarized light. When the rate of the rotational diffusion of the fluorophore is similar to emission rate, anisotropy values change according to diffusional properties, such as an increase in viscosity. Anisotropy value can reflect whether a fluorophore is in free state or in a bound state. When a fluorophore is chemically linked to a protein, fluorescence anisotropy reveals the local conformational motion of the labeled residue and can be used to probe for changes such as binding with lipid membrane or complex formation (Lakowicz, 1999). Cy3-tetrazine-labelled at 836th position of WT-S* or D614G-S* virions were used to follow the fusion peptide conformational motion by anisotropy measurements to determine whether the fusion peptide of the spike is getting inserted into the liposome during membrane fusion reaction.

Anisotropy measurements were carried out in a QuantaMaster spectrometer (Model QM8450, Horiba) with in-built polarizers. Data was collected with the FelixGx software with the integration time set at 3 s. Excitation and emission wavelengths were set to 532 nm and 570 nm and G factors were measured for every set of experiments. Virions having either Cy3 labeled WT-spike or D614G spike (fluorophore lebelling described above) were mixed with proteo-liposomes having all the receptors (hACE2/NRP1/hTMPRSS2) and incubated with buffer at pH4.6 for 5 min so that virus can bind the liposome, followed by anisotropy measurement was started. After 150 s of initiation of the recording, $CaCl_2$ solution was added in stopped-flow manner and the drastic change in anisotropy was observed, reflecting the membrane insertion of fusion peptide (Figures 4C and 4D). Anisotropy experiments were performed at wide range of calcium concentration (100uM to 10mM). All experiments were performed in at 37°C.

FRET for spike conformational change determination

FRET measurements were performed in order to monitor the SARS CoV-2 spike protein conformational change from pre-fusion state to post-fusion state due to membrane fusion, as done previously for influenza HA and Ebola GP (Das et al., 2018, 2020). Virions with either wild-type spike or D614G spike having Q836TCO* and G1035TCO* were labeled with tetrazine-Cy3 (donor) and tetrazine-Cy5 (acceptor), as described above. Donor fluorescence was measured with QuantaMaster (QM-8450, Horiba) with an excitation wavelength of 532 nm and emission was collected from wavelength 550 nm–700 nm. Virions and proteo-liposomes containing all the receptors ACE2/NRP1/TMPRSS2 were incubated, and low pH and $CaCl_2$ were added in stopped flow manner and donor fluorescence was measured. FRET efficiency was determined by comparing donor fluorescence in presence of acceptor and with respect to only donor, present in spike protein of virions. High fluorescence resonance energy transfer (High-FRET) causes lower emission intensity in donor and increase in acceptor emission intensity and low FRET increases donor emission intensity and decreases acceptor intensity (Figures 5D and 5E). FRET experiments were performed at wide range of calcium concentration (100uM to 10mM) at pH 4.6. All experiments were performed in at 37°C.

Live-cell confocal imaging

Live cell microscopy were performed on a LSM780 confocal microscope (Carl Zeiss) with a 63X/1.4 NA oil based objectives. Live cells were imaged on a heated stage maintaining the 37C temperature and 5% CO_2. Laser excitation wavelength of 488nm was used for imaging GFP-labelled TPC1/TPC2, 532nm laser was used for imaging DiD labeled pseudivirions and 647 nm wavelength laser was used for imaging LysoTracker red labeled lysosomes. Zen software (Carl Zeiss) were used for all image acquisition and analysis.

QUANTIFICATION AND STATISTICAL ANALYSIS

Statistical data throughout our study were performed using Student's t-test and are described in the respective figure legends. p values were determined by two-tailed student t test. The p value < 0.0001 were indicated as (*) and p value < 0.00001 were indicated as (**) throughout our study. The experiments were not randomized and investigators were not blinded for outcome assessment.